5-2013

Intermediate Band Solar Cells Based on InAs Quantum Dots Embedded in InGaAs Quantum Well

Ramesh Vasan
University of Arkansas, Fayetteville

INTERMEDIATE BAND SOLAR CELLS BASED ON InAs QUANTUM DOTS EMBEDDED IN InGaAs QUANTUM WELL

INTERMEDIATE BAND SOLAR CELLS BASED ON InAs QUANTUM DOTS EMBEDDED IN InGaAs QUANTUM WELL

A thesis submitted in partial fulfillment
of the requirements for the degree of
Master of Science in Electrical Engineering

By

Ramesh Vasan
Anna University
Bachelor of Engineering in Electronics and Instrumentation, 2010

May 2013
University of Arkansas

ABSTRACT

Intermediate band solar cells based on quantum dots and quantum wells with anti-reflection coating are investigated in this thesis. The demand for high efficient solar cells as an alternate source of energy is the main motivation for this research project. Intermediate band solar cells based on quantum dots were the subject of intensive research in recent years. High power conversion efficiency was predicted from InAs/GaAs intermediate band solar cells as the presence of InAs quantum dots increased the absorption below the band gap of the host material.

In this thesis, an attempt has been made to further increase the absorption of GaAs solar cells by embedding InAs quantum dots in $In_xGa_{1-x}As$ quantum wells. The quantum efficiency and spectral response measurements of quantum dots embedded in quantum well devices exhibit an extended response till 1280 nm in the near infrared region of the electromagnetic spectrum. The interband transition peaks associated with the $In_xGa_{1-x}As$ quantum well exhibit a red shift as In mole fraction (x) in $In_xGa_{1-x}As$ quantum well is increased above 0%. The short circuit current density increased, while open circuit voltage decreased, as x is increased.

In addition, the use of inexpensive anti-reflection coating (ARC) on these intermediate band solar cells has been studied. Anti-reflection coating based on Zinc oxide (ZnO) has significantly improved the power conversion efficiency of the solar cells. The ZnO synthesized using sol-gel technique was spin coated on the solar cells and subsequently annealed. The short circuit current density was significantly increased after the deposition of the ARC. Enhancement of the order of 42 % in the power conversion efficiency was obtained. Around 43% enhancement in quantum efficiency and 44% enhancement in spectral response measurements were also observed.

This thesis is approved for recommendation
to the Graduate Council.

Thesis Director:

_____
Dr. Omar Manasreh

Thesis Committee:

_____
Dr. Shui-Quing Yu

_____
Dr. Simon Ang

THESIS DUPLICATION RELEASE

I hereby authorize the University of Arkansas Libraries to duplicate this thesis when needed for research and/or scholarship.

Agreed _____

Ramesh Vasan

Refused _____

Ramesh Vasan

ACKNOWLEDGEMENTS

First of all I would like to thank my parents, my brother and sister in-law for their love and support. Without their support it would not have been possible for me to complete my graduate study.

I would like to express my deep gratitude to my graduate advisor and thesis director, Dr. Omar Manasreh for providing me an opportunity to do this research project. His guidance and support for the past two years has been invaluable in completing this project.

I am thankful to Dr. Simon Ang and Dr. Shui-Qing Yu for being in my thesis committee and helping me with the project.

I wish to thank my group members, Yahia Makableh, Jony Chandra Sarker, Dr. Scott Little, Dr. Jiang Wu, Dr. Mahmood Khan, Seungyong Lee, Scott Mangham, Ahmad Nusir, and Rick Eyi for their support and help in completing this project.

I would like to thank Dr. Vasundra Varadan and her student Sayan Seal for helping me with the ellipsometry measurements.

This work was partially supported by the Air Force Office of Scientific Research (Grant FA9550-10-1-0136), the NSF-EPSCoR program (Grant EPS-1003970), and NASA-EPSCoR program (Grant 242026-1BBX11AQ36A).

TABLE OF CONTENTS

1. INTRODUCTION…… 1

1.1. Basics of solar cells…….. 2

1.2. III-V semiconductor solar cells…… 6

1.3. Intermediate band solar cells…… 7

1.4. Anti-reflection coating……. 9

2. MATERIALS GROWTH AND DEVICE FABRICATION…….. 11

2.1. Epitaxial growth of InAs quantum dots……... 11

2.2. Synthesis of Zinc oxide by sol-gel method…….. 12

2.3. Fabrication of GaAs solar cells…… 13

2.3.1. Sample cleaning…… 13

2.3.2. Photolithography……... 13

2.3.3. Metallization……. 14

2.3.4. Lift-off……... 14

3. CHARACTERIZATION TECHNIQUES…….. 16

3.1. Material characterization……. 16

3.1.1. Transmission measurement…….. 16

3.1.2. X-ray Diffraction (XRD)…….. 16

3.1.3. Spectroscopic Ellipsometry……. 17

3.2. Device characterization…….. 18

3.2.1. IV characteristics measurement…….. 18

3.2.2. Quantum efficiency measurement…… 19

3.2.3. Spectral response measurement…… 21

4. RESULTS AND DISCUSSION…….. 23

4.1. InAs/$In_xGa_{1-x}As$/GaAs intermediate band solar cells……. 23

4.1.1. Introduction…….. 23

4.1.2. Device structure…… 23

4.1.3. Results and discussions…… 25

4.2. Anti-reflection coating for GaAs solar cells…… 31

4.2.1. Introduction…….. 31

4.2.2. Deposition and characterization…….. 31

4.2.3. Optimization of ARC films…….. 36

4.2.4. InAs/GaAs solar cells with ZnO ARC……. 37

4.2.5. InAs/$In_{0.15}Ga_{0.85}As$/GaAs solar cells with ZnO ARC…….. 41

5. CONCLUSION AND FUTURE WORK…… 44

5.1. Conclusion…….. 44

5.2. Future work…….. 44

REFERENCES…….. 46

LIST OF FIGURES

Figure 1.1 Solar radiation power spectrum is plotted as a function of wavelength at AM0 and AM1.5……..3

Figure 1.2 Equivalent circuit of a solar cell……4

Figure 1.3 IV characteristic of a GaAs pn junction solar cell is showing the maximum power point……5

Figure 2.1 Sol-gel synthesis process is explained in a step by step flow chart……..12

Figure 2.2 The power conversion efficiency and fill factor of the GaAs pn junction solar cells are plotted as s function of metal deposition temperature…….....15

Figure 3.1 A schematic of a vertically aligned spectroscopic ellipsometer with the incident and reflected light beam is shown……...18

Figure 3.2 (a) The photograph of the Oriel IQE 200 QE measurement system is shown. (b) The block diagram is showing the operation of the system…….20

Figure 3.3 (a) The Bruker HR125 FTIR spectrometer with a Janis cryostat mounted in the detector chamber. (b) The block diagram of the spectrometer is shown with the light beams……22

Figure 4.1 (a) The different layers of the InAs/$In_xGa_{1-x}As$/GaAs solar cell structure. (b) A schematic of the device with top and bottom metal contacts……24

Figure 4.2 The spectral response taken at 300 K is showing the various interband transitions. The extended infrared responses are expanded in the inset…….26

Figure 4.3 The EQE of InAs/InGaAs devices are compared to GaAs pn junction device……27

Figure 4.4 The 300 K and 77 K spectral response spectra of an InAs/GaAs device are plotted...28

Figure 4.5 IV characteristics of InAs/InGaAs devices are plotted along with the reference GaAs pn junction solar cell…….....29

Figure 4.6 Refractive index of ZnO film is compared with the calculated refractive index of an ideal ARC for GaAs substrates…….32

Figure 4.7 Extinction coefficients of GaAs and ZnO film are plotted as a function of wavelength of incident light…….33

Figure 4.8 XRD peaks showing the presence of ZnO in the ARC film on GaAs substrate……..34

Figure 4.9 Transmission spectra of undoped GaAs samples with ZnO ARC spin coated at different speeds. ……..35

Figure 4.10 Reflectance of light from pristine GaAs and GaAs coated with ZnO ARC measured at an angle of incidence of 15^{o} ……..……..36

Figure 4.11 Performance of GaAs pn junction devices are plotted as a function of ARC film coating speed……...37

Figure 4.12 Current-Voltage characteristics of InAs/GaAs solar cell showing the enhancement after ZnO ARC deposition. ……...39

Figure 4.13 (a) Enhancement in EQE and (b) enhancement in spectral response of InAs/GaAs solar cell after ZnO ARC deposition…….40

Figure 4.14 Enhancement in the IV characteristics of InAs/ $In_{0.15}Ga_{0.85}As$ quantum dots in well solar cell with ZnO ARC……42

Figure 4.15 (a) Quantum efficiency and (b) spectral response enhancement in InAs/$In_{0.15}Ga_{0.85}As$ quantum dots in well solar cell with ZnO ARC……..43

1. INTRODUCTION

The depletion of fossil fuels and the demand for more renewable energy sources has opened up new possibilities for tapping energy from the sun. Solar cells based on semiconductors have been studied for a long time for their use as sustainable energy resources. Several improvements have been made in this field in the past years. But the efficiency of these devices is less when compared to other non-renewable energy sources. Several different types of solar cells made from different semiconductors have been studied to increase the efficiency.

One of the main approaches that have been adopted is the use of low dimensional nanostructures such as quantum wells and quantum dots in the active region of the solar cells. These semiconductor nanostructures have unique properties when compared to their bulk counterparts. Specifically, quantum dots have three dimensional carrier confinement and also increase the absorption of the solar cells below the band gap of the host material. This makes them suitable for high efficient solar cell applications. In this project solar cells based on quantum dots embedded into quantum wells have been studied. The main idea behind the introduction of quantum wells is to increase the absorption in the near infrared region. Also, the effect of anti-reflection coating (ARC) on these solar cells has been studied.

In chapter 1 the basic operating principles of solar cells, current progress in quantum dot solar cells and the basics of solar cell ARC have been discussed. Chapters 2 and 3 discuss the solar cell fabrication process and the tools used to characterize them. Chapter 4 analyses the performance of quantum dots in quantum well solar cells and the effect of ARC on these solar cells. Finally, in chapter 5 the project is concluded and the possible future works are proposed.

1.1 Basics of Solar cells

Sunlight is a form of electromagnetic radiation, which is composed of particles called photons. Each photon is associated with a particular wavelength and energy given by:

$$E = \frac{hc}{\lambda} \tag{1.1}$$

where, E is the energy, h is the Planck's constant, c is the speed of light and λ is the wavelength of light. When light is incident on a semiconductor, a part of it is absorbed by the current carriers namely electrons and holes. All semiconductors are associated with a band gap, given in terms energy in electron volts (eV). Only those photons with energies higher than the band gap of semiconductor are absorbed and carriers are generated. Those photons with lesser energy just pass through the semiconductor and do not involve in carrier generation. The carriers thus generated must be separated before they recombine. A semiconductor diode absorbs the photon, generates the carriers, and separates them before they recombine. Thus, a solar cell is semiconductor diode designed in such a way that it can absorb light efficiently and generate carriers.

All the radiation emitted by the sun does not reach the earth, only a part of it reaches the earth. The radiation intensity just above the earth is about 135.3 mW/cm^2 and this spectral distribution is referred as air mass zero (AM0). Air mass is the measure of intensity reduction as the radiation passes through the earth's atmosphere. The air mass number is given by [1]:

$$\text{Air mass} = \frac{1}{\cos\theta} \tag{1.2}$$

where, θ is the angle of incidence on the earth's surface. The standard used to evaluate the performance of a solar cell is AM1.5. The angle of incidence at this standard is 48.2^o, which is calculated using the above equation. The total radiation intensity at this standard is 100 mW/cm^2. The solar radiation spectrum at AM0 and AM 1.5 is shown in figure 1.1 [2].

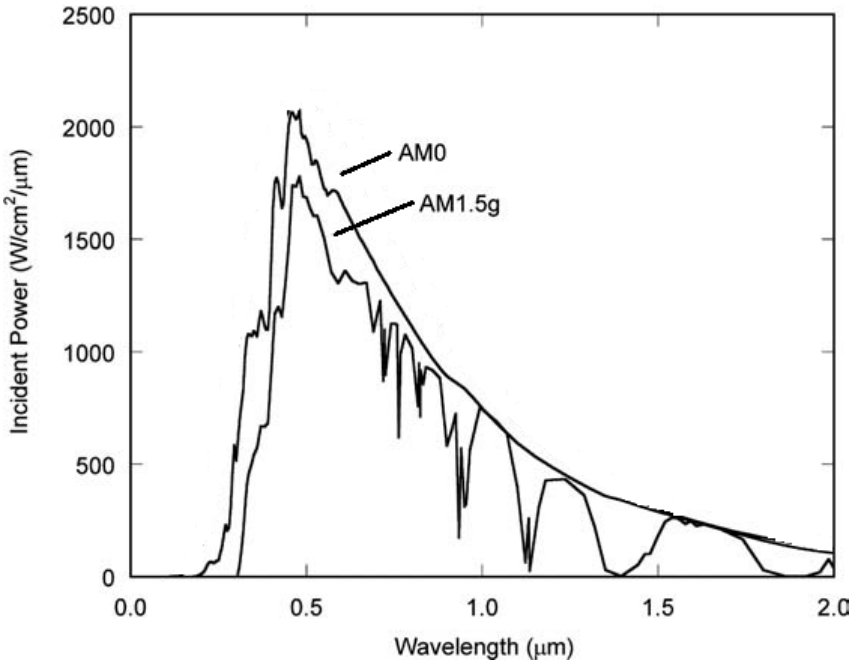

Figure 1.1 Solar radiation power spectrum is plotted as a function of wavelength at AM0 and AM1.5.[2]

As seen from figure 1.1, the intensity of the solar spectrum at AM1.5 is highest in the visible range (400 nm to 700 nm). Hence, a good solar cell is designed in such a way that it can absorb maximum number of photons in the visible wavelength range.

The operation of the solar cell is similar to that of pn junction diode. The current-voltage (IV) characteristic of pn junction diode is given by:

$$I = I_0 \left[\exp(\frac{qV}{nkT})\right] - I_0 \tag{1.3}$$

where, I is the current, I_0 is the saturation current, q is the charge, k is the Boltzmann constant, T is the temperature and n the ideality factor of the diode. A solar cell can be modeled in such a way that a current source is connected across a pn junction diode, with the current flowing in a

direction so as to make the diode forward biased. The equivalent circuit of a solar cell is shown figure 1.2.

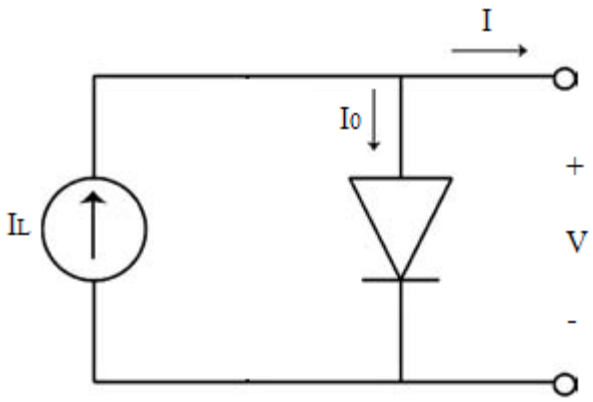

Figure 1.2 Equivalent circuit of a solar cell.

Under no light condition the solar cell behave as a normal pn junction diode and IV characteristics of the device follows equation 1.3. The current generated is called dark current. Under illumination electron hole pairs are generated and collected. The additional current generated due to absorption of light is called photocurrent. In this condition the diode IV characteristic is given by:

$$I = I_L - I_0 \left[\exp(\frac{qV}{nkT})\right] - I_0 \tag{1.4}$$

where, I_L is the photocurrent. The IV characteristics of typical GaAs pn junction solar cell under dark and illuminated conditions is shown in figure 1.3.

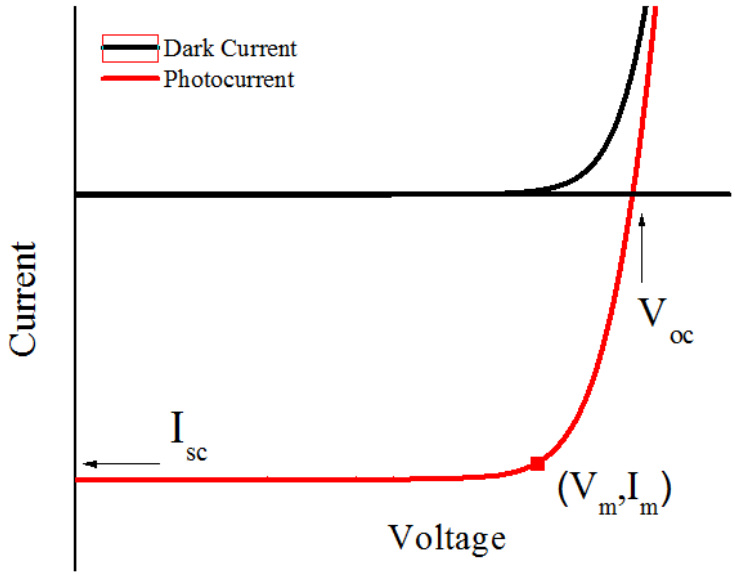

Figure 1.3 IV characteristic of a GaAs pn junction solar cell is showing the maximum power point.

The current at which the voltage is zero is called the short circuit current of the solar cell, denoted by I_{sc}. The voltage at which the current becomes zero called open circuit voltage, denoted by V_{oc}. The maximum power point or the operating point of the solar cell is indicated by a square in figure 1.3. The voltage and current at the maximum power point is denoted by V_m and I_m respectively. The performance of the solar cell is evaluated by two important factors namely power conversion efficiency (η) and fill factor (FF). The power conversion efficiency is the ratio of product of voltage and current at the maximum power point to input solar power. The fill factor describes the closeness of the solar cell to an ideal solar cell which has a fill factor of unity. η and FF a solar cell is given by the following equations:

$$\eta = \frac{V_m I_m}{P_{in}} \times 100\% \qquad (1.5)$$

$$FF = \frac{V_m I_m}{V_{oc} I_{sc}} \tag{1.6}$$

As the V_{oc} of the solar cell depends on the band gap of the material, the efficiency of the solar cell also depends on the band gap of the solar cell. The optimum band gap for power generation at a solar radiation spectrum of AM1.5 is found to be 1.5 eV [3]. Compound semiconductors like gallium arsenide (GaAs), indium phosphide (InP), cadmium telluride (CdTe) and copper indium disulfide ($CuInS_2$) have band gaps closer to the optimum value [1][4][5]. In general for solar cell applications semiconductors with band gap in the range of 1.0 – 1.7 eV are used [6].

1.2 III-V compound semiconductor solar cell

Solar cells made from III-V semiconductors such as GaAs, InP and GaSb have the possibility of achieving high efficiency as these materials have direct band gap, high absorption coefficient and longer minority carrier life time and mobility [3]. The band gaps of GaAs and InP are 1.43 eV and 1.34 eV respectively, which are closer to the optimum value. Hence, they are the most widely used III-V semiconductors for solar cell applications. Specifically GaAs, apart from having high carrier mobility, has low power dissipation due to reduced series resistance, high minority carrier diffusion lengths and reduced surface recombination [7]. The high absorption coefficient of GaAs leads to increased surface recombination, which is detrimental for solar cell applications. But at a high carrier concentration of around ~$10^{18}/cm^3$, the electron mobility becomes high, which leads to reduced surface recombination [8]. The high absorption coefficient of GaAs makes it possible to fabricate thin film solar cells, as 95 % of the photons are absorbed within 3 um of the cell [7]. Generally these devices are grown using liquid phase epitaxy and metal organic chemical vapor deposition. High quality wafers from III-V

semiconductors for solar cell applications are grown using molecular beam epitaxy (MBE) these days.

Theoretical efficiency of a single junction GaAs solar cell was found to be as high as 39 % [6]. An efficiency of about 11 % was reported for one of the first GaAs solar cell [7]. Even though the III-V semiconductor solar cells had the potential for producing high efficiencies, there are certain drawbacks associated with them. The first drawback is the high cost of production of high quality substrates and epitaxial layers for photovoltaic applications. The other drawback is the susceptibility of these materials to defects and other crystal impurities. In a single junction solar cell the photons with energies higher than the band gap does not generate carriers, which leads to a decreased efficiency. Hence, multi junction solar cells made of materials with different band gaps were used. The materials are stacked such that photons with different energies are absorbed and carriers are generated. High theoretical efficiency on the order of ~ 60 % by stacking number of cells was reported [9, 10].

1.3 Intermediate band solar cells

The theoretical efficiency of single junction solar cells described previously under full concentration is ~ 40.7 % [11], [12]. This is due to the fact that only those photons with energies closer to the band gap of the solar cell material are converted into electric power. One approach to increase the absorption and hence the power conversion efficiency is the intermediate band solar cells (IBSC) [13]. The theoretical limiting efficiency of an IBSC is predicted to be as high as ~ 63 % [13]. An IBSC consists of an intermediate band (IB) material sandwiched between the p-type and n-type material of a conventional single junction solar cell. These IB materials introduce energy levels between the valence band (VB) and the conduction band (CB) inside the

band gap of the host material. Hence, photons with energies lower than the band gap are also absorbed and electrons from the VB are excited to the CB via the IB. As a result the photocurrent of an IBSC is higher when compared to the conventional solar cell. Increase in photocurrent can also be achieved by using a material of lesser band gap so as to absorb higher number of photons. But the V_{oc} of such cells are less, as the V_{oc} is directly proportional to the band gap of the semiconductor. Hence, the main idea of introducing IBSC is to increase the photocurrent without effectively reducing the V_{oc}.

The photons emitted as a result of carrier recombination between any two of the three bands can be absorbed by other carriers, which can affect the operation of the IBSC [14]. This is eliminated when the absorption between any two bands does not overlap with another pair of bands [13]. But if the absorption coefficients of the materials have a large difference in the overlapping wavelengths then a thick layer of IB material with low absorption efficient has to be used [15]. The equivalent circuit of an IBSC has been reported by Luque *et al* [16].

Several research groups have been working with InAs quantum dots based solar cells for their potential to give high power conversion efficiency. The InAs quantum dots introduce quantized energy levels, which are theorized to form the intermediate band. In terms of energy this theorized intermediate band lies between the band gap of the host material. The high power conversion efficiency was predicted as additional carriers undergo transitions through the intermediate band [17]. The presence of InAs quantum dots in the active region of a GaAs pn junction solar cell produced extended spectral response beyond the band gap of GaAs in the near infra-red region [18]. The introduction of strain compensation layers in InAs quantum dot solar cells resulted in high V_{oc} of about 1.0 V [19], [20]. A. Hospodkova *et al* reported the use of $In_xGa_{1-x}As$ as strain reducing layer in InAs/GaAs devices [21]. High density of quantum dots

[22], [23] and presence of energy fence barriers [24], [25] were reported to have increased the performance of InAs quantum dot devices.

1.4 Anti-Reflection coating

The photons that are incident on the solar cells are not completely absorbed. There is radiation loss which results in lowering the I_{sc}. One of the major optical losses is the reflection of light from the surface of the solar cell. Optical losses can be minimized by ARC, surface texturing to increase the path length of light and light trapping. Out of these, ARC is the most widely used method to reduce optical losses. These are thin coating of a suitable dielectric material with a particular refractive index and thickness. The refractive index and thickness of the coating has to be chosen carefully so that the light reflecting from the top of the ARC and the top of the solar cell surface undergo destructive interference. Hence, net energy lost is zero. For an ideal ARC, the thickness of the coating should be less than one fourth of the wavelength of interest. Also, the refractive index of the ARC should be equal to the geometric mean of refractive index of air (n_{air}) and the refractive index of the semiconductor substrate ($n_{substrate}$).

$$n_{ARC} = \sqrt{n_{air} n_{substrate}} \tag{1.7}$$

Generally, solar cells are active in the wavelength range of 400 nm to 800 nm. Hence, the thickness and refractive index of the ARC are chosen so that reflection is reduced in this wavelength range.

Single layer, bilayer and multilayer ARC have been used for solar cells. Specifically, surface modification and texturing by ARC have been well studied for silicon solar cells. The blue colour of commercially available silicon solar cells is due to deposition of silicon nitride

ARC. These films are grown by Chemical vapour deposition. Surface texturing by submicron antireflection structures on GaAs solar cells has been reported [26]. The use of zirconium oxide /aluminum oxide bilayer ARC and conducting tin oxide nanocolumns on GaAs solar cell have also been reported [27],[28].

2. MATERIALS GROWTH AND DEVICE FABRICATION

2.1 Epitaxial growth of Quantum Dots

Molecular Beam Epitaxy (MBE) is an advanced growth system specifically used to grow compound semiconductors. Usually semiconductor nanostructures for optoelectronic and photovoltaic applications are grown using MBE. The structures are grown on a substrate layer by layer epitaxially on a substrate. The system operates at ultra-high vacuum, which results in high quality materials. The sources are introduced through the effusion cells, which are heated slowly. The heated elements evaporate and are deposited on the substrate one layer over the other. Deposition rates are typically 1- 2 monolayers per second. The slow deposition rate enables high control over the growth. The system is equipped with a number of in-situ measurement units to control the growth parameters. In this project, the quantum dots in quantum well solar cells were grown using MBE.

Epitaxial growth can be of the following three modes. Volmer-Weber mode or island mode, Frank-Van de Merwe mode or layer mode and Stranski-Krastanov mode, which is a combination of both island and layer modes [29]. The InAs quantum dots in the solar cells used in this project were grown using Stranski-Krastanov growth mode. In this two or three monolayers of InAs are grown on the GaAs buffer layer. This layer is often called as wetting layer. The lattice mismatch between InAs (lattice constant = 6.0564 Å) and GaAs (lattice constant = 5.6532 Å) causes strain to accumulate. This accumulated strain is released by forming three dimensional islands over the film. These are called quantum dots. The size and density of the quantum dots can be controlled by varying the MBE growth parameters [30].

2.2 Synthesis of Zinc Oxide using sol-gel method

Zinc Oxide (ZnO) ARC in this project was synthesized using sol-gel technique [31-35]. In this method, Zinc acetate dihydrate is used as the precursor, monoethanolamine is used as the stabilizer and isopropyl alcohol is used as the solvent. The concentration of the zinc precursor and the stabilizer must be maintained at a ratio of 1:1. One Molar solution of the zinc precursor is prepared by dissolving 2.19 gms of the salt in 10 ml of iso propyl alcohol. This solution is heated for 15 mins on a hot plate at a temperature of 50 ^{o}C. The salt dissolves in the solvent and forms a thick white cloudy precipitate. To this 1M monoethanolamine solution, prepared by dissolving 1 ml of monoethanolamine in 10 ml of isopropyl alcohol, is added and stirred for 2 hrs. The temperature of the hot plate is maintained at 50 ^{o}C. The formation of a clear solution indicates the completion of the reaction. The resulting clear ZnO sol-gel is aged for 24 hrs before it is used as an ARC for solar cells.

Figure 2.1 Sol-gel synthesis process is explained in a step by step flow chart.

2.3 Fabrication of GaAs solar cells

The solar cells were fabricated in a class 100 clean room using standard lithography procedures. The whole fabrication process can be divided into following major steps:

2.3.1 Sample cleaning

The wafers grown using molecular beam epitaxy are diced into smaller rectangular pieces. The samples are first soaked in acetone for 3 minutes, rinsed with deionized (DI) water and dried with nitrogen gas. The dried samples are then soaked in methanol for 3 minutes, rinsed and dried. Both acetone and methanol being strong organic solvents removes most of the organic impurities from the surface.

2.3.2 Photolithography

The samples are etched to from 3 mm X 3 mm square mesas, which form separate solar cell devices. In order to form the mesas, the sample has to be patterned using positive photoresist and photo mask. The cleaned samples from previous step are spin coated with AZ® P4330 positive photoresist. The coated samples are then cured at 110 ^{0}C for 3 minutes on a hot plate. The cured samples are then exposed to UV light under a positive photo mask to from the square pattern. The UV light exposed samples are developed using AZ® 400K developer. The developed samples are etched using GaAs etchant to form individual devices with an area of 3 mm X 3 mm. The surface of each device and the etch profile are characterized using an optical profiler. The etch profile and the etch depth measured using a Taylor Hobson optical profiler is shown in the figure. The etched mesas are then patterned using a second mask to for metal deposition. Just before metallization the device surface was cleaned with a solution of HCl:

H_2O, rinsed with DI water and dried with nitrogen. This was done to remove any oxide layer formed on the GaAs surface.

2.3.3 Metallization

The contact metals for both p type and n type GaAs were deposited using Angstrom Nexdep electron beam evaporator. A typical n type metallization consists of AuGe/Ni/Au with a thickness of 75 nm/20 nm/100 nm [36]. A typical p type metallization consists of Au/Zn/Au with a thickness of 100 nm/20 nm/100 nm [36]. The metal films were deposited under a vacuum of $2x10^{-6}$ Torr at a deposition rate of 0.1nm /second. In order to avoid the thermal stress due to rapid thermal annealing done to form Ohmic contacts, the samples were heated during the metallization process. The metallization process was optimized by depositing at different temperatures. The IV characteristics of different GaAs pn junction solar cells for different deposition temperature are shown in figure 2.1. These devices were fabricated from the same wafer using similar fabrication conditions. It was found that the devices with metals deposited at 100 ^{0}C performed better than other devices with a power conversion efficiency of ~12 %.

2.3.4 Lift off

After metallization, lift-off was performed on the metal films to form the contact pattern. In order to perform the lift-off, the samples are immersed in acetone and agitated in an ultrasonic bath to remove the excess metal forming the desired pattern.

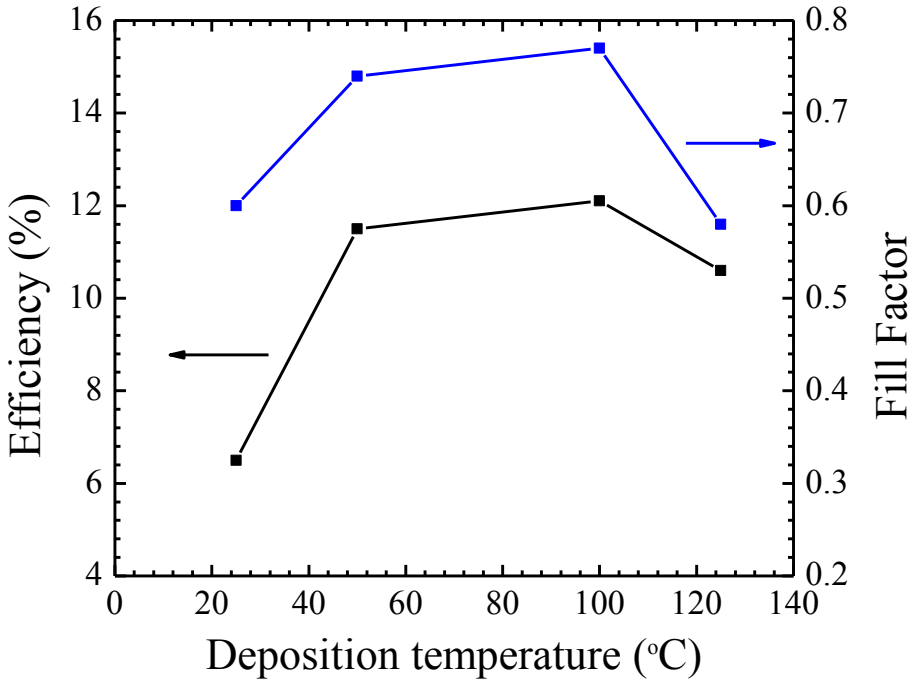

Figure 2.2 The power conversion efficiency and fill factor of the GaAs pn junction solar cells are plotted as s function of metal deposition temperature.

3. CHARACTERIZATION TECHNIQUES

3.1 Material Characterization

3.1.1 Transmission measurement

When light is incident on a semiconductor surface all photons with energies higher than the band gap energy are absorbed. Some of the incident photons are reflected from the surface and the rest are transmitted. An Ultraviolet-visible (UV-Vis) spectrophotometer is a device used to measure the absorbance, reflectance and transmittance. In this project a Cary 500 UV-Vis spectrophotometer was used to measure the transmission of light through GaAs substrate coated with an ARC. The spectrometer can scan in the wavelength range of 175 nm – 3300 nm. It consists of a photomultiplier tube detector for UV-Vis region and a PbS detector for the infrared region.

3.1.2 X-ray Diffraction

X-ray Diffraction (XRD) is a contact less material characterization technique used to identify elements, lattice spacing, crystal structures, and crystal orientation. In a crystalline structure atoms are arranged in a periodic three dimensional lattice. The space between two adjacent lattice point is called the lattice constant of the crystal. When a beam of high energy x-ray is incident on a crystal, they are scattered elastically from different planes of the crystal. This is called Thomson scattering. In this process the electrons oscillate at the same frequency of the incoming x-ray beam. The scattered x-ray beams from different lattice planes undergo interference, which are recorded as diffraction pattern. The spacing and intensity of the diffraction pattern are analyzed to determine crystal structure, and identify elements. The patterns are analyzed using Bragg's law.

The presence of ZnO in the sol-gel synthesized for ARC was confirmed using XRD. The samples were measured using Philips PW 3040 X'PERT MRD High Resolution XRD. The results obtained were compared with the materials library to identify and confirm the presence of ZnO.

3.1.3 Spectroscopic Ellipsometry

Ellipsometry is an optical measurement technique used to investigate the electrical, optical and morphological properties of thin films. It uses elliptically polarized light to find the dielectric function of the material. The dielectric function can be used to calculate the above mentioned properties. It measures the change in polarization of the light reflected from the sample. The characteristics of the polarized light reflected off the sample are dependent on the properties of the sample. Usually, an ellipsometer consists of a source, a polarizer and a compensator on the one side, which is the source side. The detector side consists of a compensator, an analyzer and a detector. The light that is parallel to the plane of incidence is called *p*-polarized light and the light that is perpendicular to the plane is called *s*-polarized light

Generally, an ellipsometer does not measure the dielectric function directly. It measures only the ellipsometric parameters namely; the amplitude component Ψ and the phase component Δ of the complex reflectance ratio of the system. The complex reflectance ratio is defined as the ratio of normalized amplitude of *p* polarized light and *s* polarized light. Even the Ψ and Δ values cannot be interpreted directly. These experimental values have to be fitted to a model using an iterative procedure to obtain the optical constants of the material. In this thesis, a J. A. Woolam VASE ellipsometer was used to measure the optical constants and reflectance of ZnO ARC. A simple schematic of a vertical ellipsometer is shown in figure 3.1.

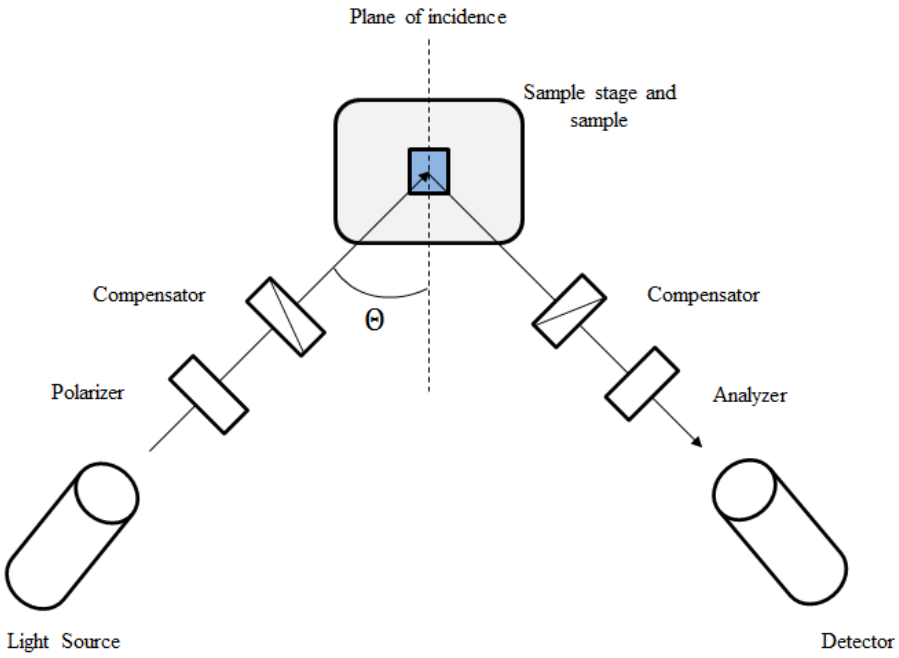

Figure 3.1 A schematic of a vertically aligned spectroscopic ellipsometer with the incident and reflected light beam is shown.

3.2 Device Characterization

3.2.1 IV Characteristics measurement

The IV characteristics of the solar cells were measured using a using Keithley SCS 4200 semiconductor characterization system in conjunction with a 300 mW/cm^2, AM1.5 solar simulator. The characterization system consists of a source measuring unit (SMU), which forces and measures the solar cell simultaneously. The voltage sweep is applied across the solar cell through one pair of leads and the current through the cell is measured by another pair of leads. This set up is typically a four point measurement to increase the accuracy by eliminating the lead resistance.

3.2.2 Quantum Efficiency

Quantum efficiency is one of the important parameter of a solar cell. Quantum efficiency is defined as the ratio of number carriers generated per incident photon of particular wavelength. In case of an ideal solar cell the quantum efficiency curve is a square with a quantum efficiency of unity. Quantum efficiency drops to zero below the band gap of the material. In case of a practical solar cell the quantum efficiency is reduced due to reflection losses, front and back surface recombination and low diffusion lengths in the bulk of the solar cell.

Generally, quantum efficiency measurements are divided into two types, external quantum efficiency (EQE) and internal quantum efficiency (IQE). EQE measurements include the optical losses like reflection and transmission while calculating the quantum efficiency of the solar cell. But IQE measurements take only the photons that are absorbed into consideration while calculating the quantum efficiency. The value of EQE of a solar cell is always lesser than the IQE value. In this project only EQE measurements were made to characterize the solar cells.

The EQE measurements were performed using a Newport IQE 200 measurement system. The photograph of and a block diagram of the measurement system is shown in figure 3.2. The instrument consists of a white light source which is chopped at a frequency of 30 Hz and passed through a monochromator. A lock-in amplifier is used to lock-in at this frequency so that only signals at this frequency are detected. The light from the monochromator hits beam splitter, part of the light goes into the reference detector and part of the light is incident on the solar cell. Another detector measures the reflected light from the solar cell surface. From these measurements the EQE is calculated using:

$$QE(\lambda) = \frac{hc}{\lambda} \frac{S(\lambda)}{q} \tag{3.1}$$

where, $S(\lambda)$ is the power spectral responsivity.

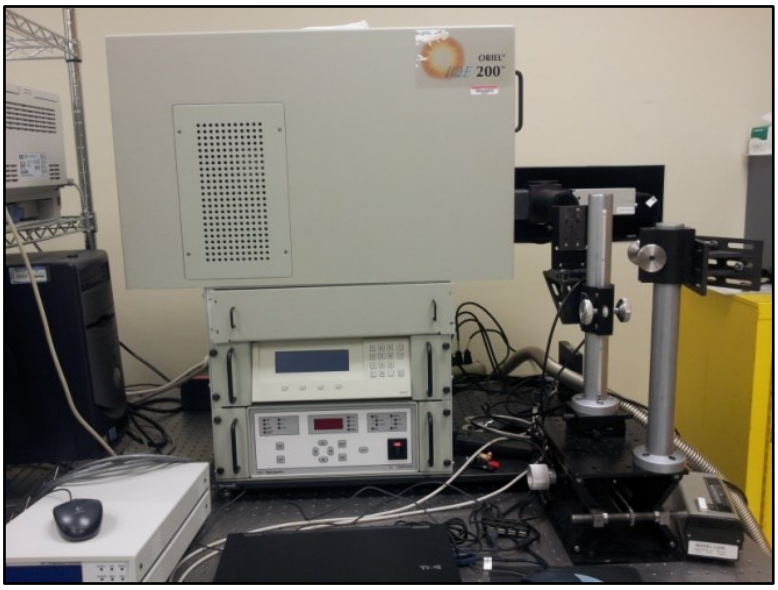

(a)

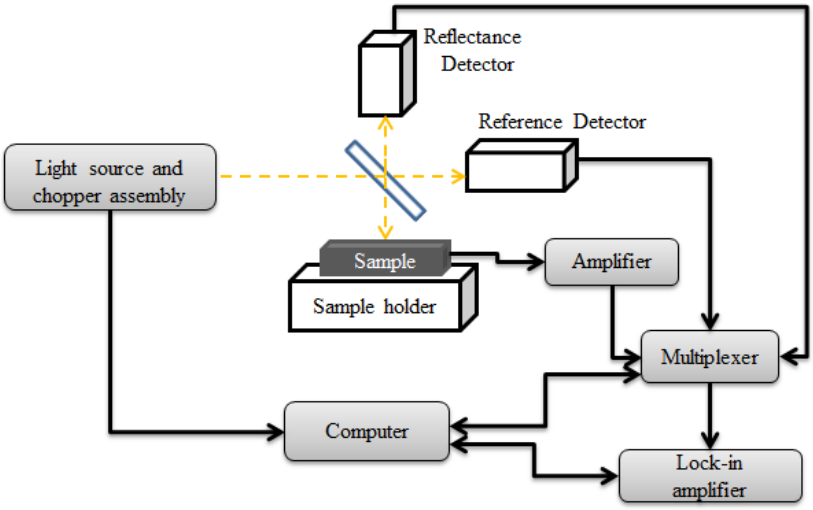

(b)

Figure 3.2 (a) The photograph of the Oriel IQE 200 QE measurement system is shown (Photograph taken by Ramesh Vasan). (b) The block diagram is showing the operation of the system.

3.2.3 Spectral Response measurement

The spectral response is similar to that of quantum efficiency, except that spectral response is defined as the ratio of I_{sc} to the power of incident photon of particular wavelength. In other words, it is a measure of how well the solar can absorb a photon of particular wavelength and generate electron that contribute to the I_{sc}. Similar to quantum efficiency, the spectral response curve drops to zero just above the band gap of the material.

The spectral response in this project was measured using a Bruker 125HR Fourier transform infrared (FTIR) spectrometer in conjunction with a Keithley 428 current preamplifier. A FTIR spectrometer is generally used to measure both absorption and emission spectra. It consists of a Michelson Interferometer, a broadband light source and a detector based on the application. The interferometer consists of beam splitter, one fixed mirror and another movable mirror. The light reflected from the fixed and movable mirror interfere and this output of the interferometer is called the interferogram. The output changes with every position of the movable mirror, which is transformed into spatial coordinate using Fourier transform. A HeNe laser is used to track the movement of the movable mirror. A quartz beam splitter and a quartz halogen source were used. The quartz halogen source has a range of 5000 cm^{-1} to 25000 cm^{-1}. The solar cells were used as the detector mounted on a Janis Cryostat. The sample chamber pressure was maintained at ~10^{-6} Torr. Low temperature measurement was carried out using liquid nitrogen and Lakeshore 311 temperature controller. The spectrometer setup and its block diagram are shown in the figure 3.3.

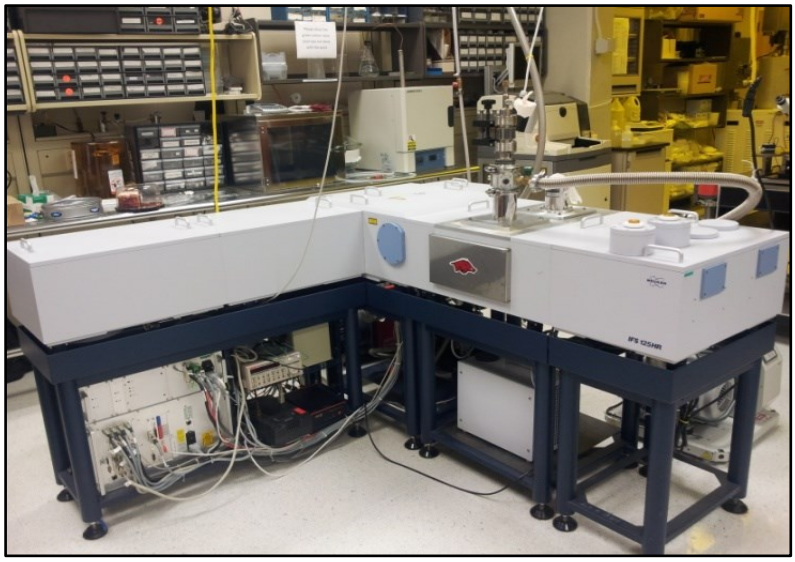

(a)

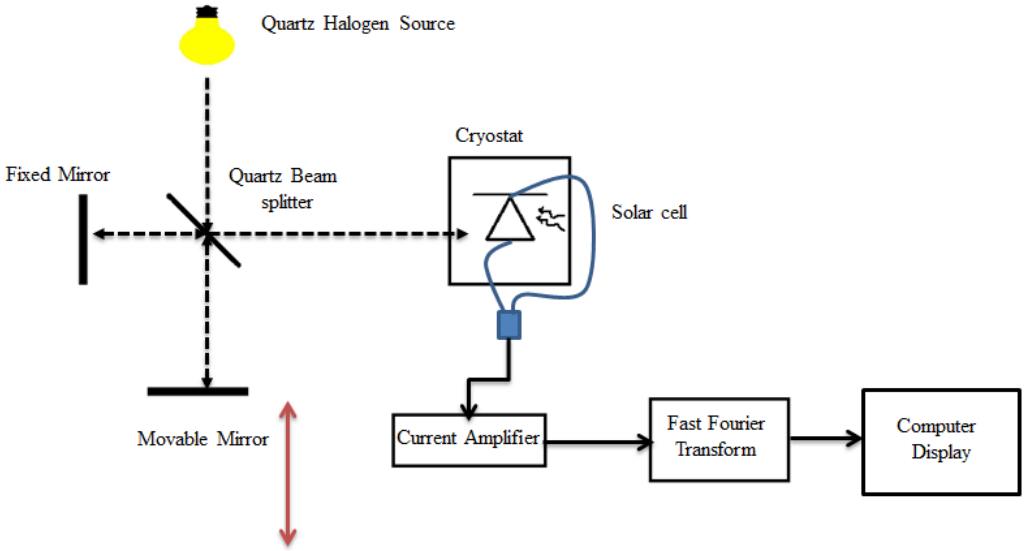

(b)

Figure 3.3 (a) The Bruker HR125 FTIR spectrometer with a Janis cryostat mounted in the detector chamber (Photograph taken by Ramesh Vasan). (b) The block diagram of the spectrometer is shown with the light beams.

4. RESULTS AND DISCUSSIONS

4.1 InAs/$In_xGa_{1-x}As$/GaAs intermediate band solar cells

4.1.1 Introduction

Intermediate band solar cells based on InAs have been the area of intensive research in recent years [17-25]. The presence of InAs quantum dots increases the short circuit current density (J_{sc}) and also extends the response of the solar cell. In this project, solar cells based on InAs quantum dots embedded into $In_xGa_{1-x}As$ quantum wells with GaAs barrier have been investigated. The main idea of embedding the InAs quantum dots into $In_xGa_{1-x}As$ quantum wells is to extend the response of the solar cells further into the infrared region. The In mole fraction (x) was varied between 0 – 0.4 to engineer the position of the intermediate band within the band gap of GaAs.

4.1.2 Device structure

The nanostructures were grown by MBE [18]. The different layers of the device structure and the schematic of the device are shown in figure 4.1 (a) and (b) respectively. Ten periods of 2ML InAs quantum dots/5nm of $In_xGa_{1-x}As$ quantum well/35nm GaAs barrier was grown on an n-type GaAs substrate. The InAs quantum dots were doped with [Si] = $2x10^{17}$ cm^{-3}. The quantum dots were n-doped in order to provide partially filled intermediate band, which allows transition of carriers via the intermediate band [37]. The ten period structure was embedded into the depletion region of the GaAs pn junction. An n-type buffer layer was grown on top of the substrate, which was doped with [Si] = $5x10^{18}$ cm^{-3}. The InAs /$In_xGa_{1-x}As$/GaAs structure was capped with a p-type GaAs cap layer doped with [Be] = $1x10^{18}$ cm^{-3}. A 100 nm thick n-type $Al_{0.2}Ga_{0.8}As$ doped with [Si] = $1x10^{18}$ cm^{-3} was inserted in the buffer layer, which

acts as the back surface field. A 40 nm p-type $Al_{0.85}Ga_{0.15}As$ doped with [Be] = $1x10^{18}$ cm^{-3} was inserted in the cap layer which acts as the window layer. The p-type AlGaAs window layer passivates the p-type GaAs surface states, which acts as minority carrier traps. This reduces the front surface recombination, which degrades the performance of the solar cell. Similar to the window layer, the n-type back surface field passivates the interface between the base and the tunnel-junction interconnects. The mole concentration of Al is chosen in such a way that VB and CB offset ratio of AlGaAs to GaAs is large.

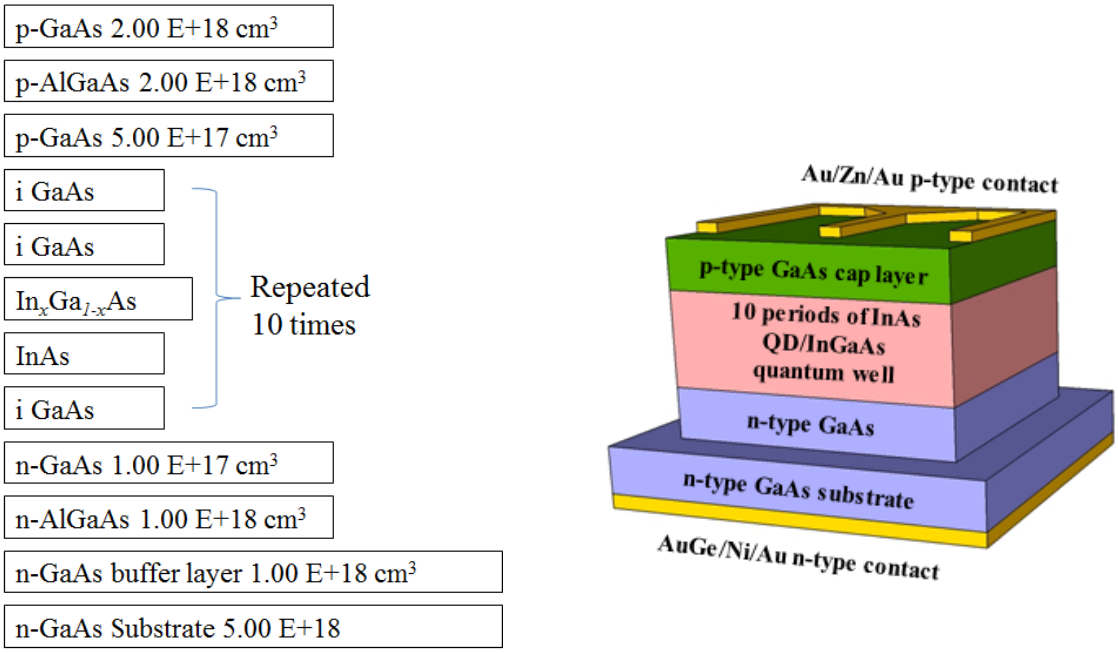

Figure 4.1 (a) The different layers of the InAs/$In_xGa_{1-x}As$/GaAs solar cell structure. (b) A schematic of the device with top and bottom metal contacts.

4.1.3 Results and Discussions

Five different wafers containing structures with x = 0%, 10%, 15%, 25% and 40% were grown. Solar cell devices of size 3 mm X 3 mm were fabricated from these wafers using the fabrication process described in the previous chapter. A reference wafer containing a GaAs pn junction was also grown and devices were fabricated out of it as well. The room temperature spectral response spectra of these devices were measured and are plotted in figure 4.2. The rapid decay in the spectral response below 700 nm is due to the response of the quartz beam splitter in the spectrometer. The strong peak at 867 nm seen in all the spectra is due to the interband transition in the GaAs. The transition of electron from the CB to VB is called interband transition. The weaker peak at 920 nm seen in all the spectra except for the reference cell is due to transition associated with the InAs quantum dot. The peaks between 950 nm and 1020 nm seen in devices with x = 10 %, 15 % and 25 % are interband transitions associated with $In_xGa_{1-x}As$. The interband related peaks can also be observed in the external quantum efficiency spectra as shown in figure 4.3. The red-shift of these interband transition peaks seen in both spectral response and external quantum efficiency is due to the decrease in the band gap of $In_xGa_{1-x}As$ quantum well as the x is increased according to the following room temperature band gap equation [38]:

$$E_g = 0.4362x^2 - 1.5012x + 1.425 \quad (4.1)$$

where E_g is the band gap of $In_xGa_{1-x}As$. The spectral response of the device with x = 40 % is severely degraded due to the excessive strain induced dislocations caused by the lattice mismatch between GaAs and $In_{0.4}Ga_{0.6}As$.

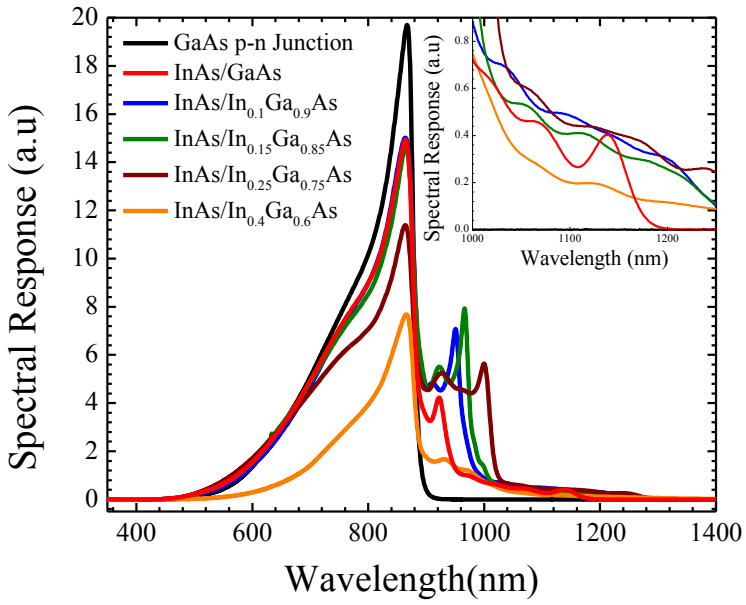

Figure 4.2 The spectral response taken at 300 K is showing the various interband transitions. The extended infrared responses are expanded in the inset.

The external quantum efficiency depends on the spectral responsivity of the device, but they represent different aspects of the devices. The external quantum efficiency gives the number of electrons excited per incident photon, which is an important parameter used to calculate the power conversion efficiency of the solar cell. The quantum efficiency of InAs/InGaAs devices is improved below 700 nm when compared to the reference GaAs pn junction device. The improvement below 700 nm may be explained by the presence of the transitions from bound states to the continuum and by transitions related to X or L minima in the InAs quantum dots. Also, there was a decrease in quantum efficiency between 700 nm and 900 nm. This reduction can be attributed to the strain induced defects generated at the interfaces of GaAs and InGaAs layers.

In addition to these strong interband transitions, there are several low energy transitions in the spectral response spectra as indicated in the inset of figure 4.2. Similar low intensity peaks were reported in InAs quantum dot devices [18]. These peaks are seen only in measurements performed at 300 K and disappear at 77 K. This shows that these low energy transitions are thermally assisted. The spectral response of InAs/GaAs device taken at 300 K and 77 K is shown in figure 4.4. It can be noted that these transitions disappear at 77 K. The current generated by these transitions are very less and does not enhance the efficiency.

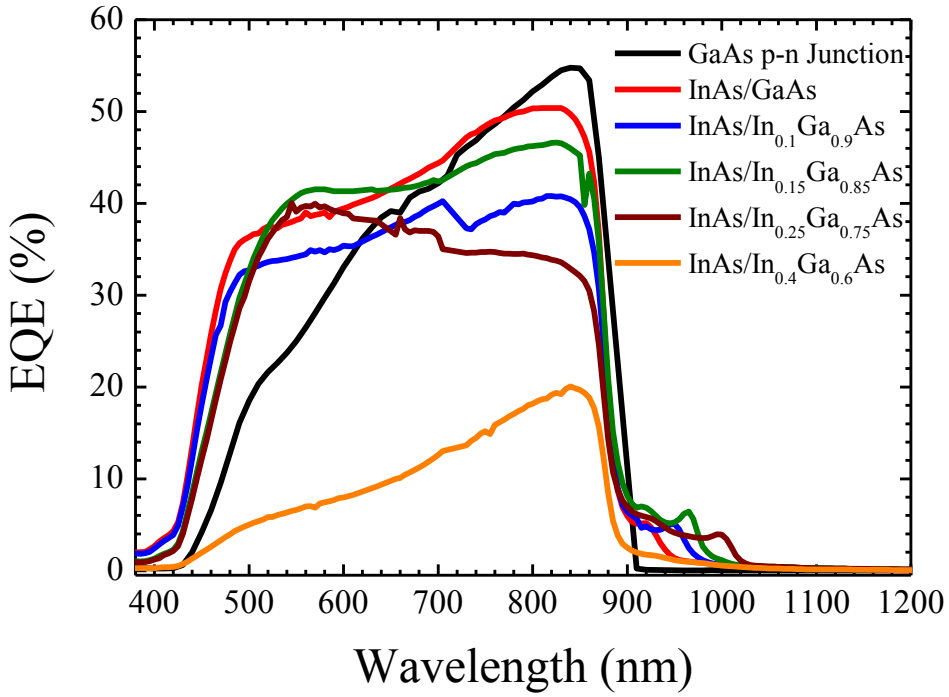

Figure 4.3 The EQE of InAs/InGaAs devices are compared to GaAs pn junction device.

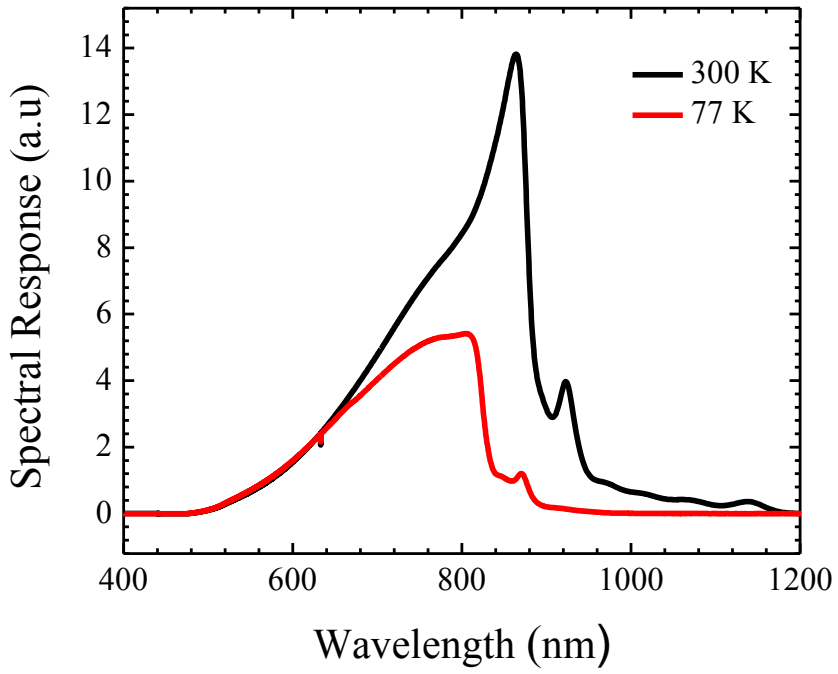

Figure 4.4 The 300 K and 77 K spectral response spectra of an InAs/GaAs device are plotted.

The IV characteristics of InAs/InGaAs devices plotted along with the reference GaAs pn junction device are shown in figure 4.5. It can be noted that the J_{sc} increased as the *x* is increased from 0 % to 25 %. The interband transitions, which are absent in the reference GaAs solar cell, is the main cause for the increase in the J_{sc}. The increase in photocurrent can also be explained as due to the carrier tunneling through the intermediate band. Carrier tunneling through intermediate band was also reported by Shang *et al* [39]. Thermal generation of carriers and tunneling through defects are other possible causes for the increased photocurrent. The increase in J_{sc} was accompanied by decrease in the V_{oc}, which resulted in the overall decrease in the power conversion efficiency. It can also be observed that the fill factor is decreased for InAs/InGaAs devices. As seen from the IV characteristics, the performance of the device with *x* = 40 % was greatly decreased. This can be attributed to strain induced defects caused by the

increased lattice mismatch between GaAs and InGaAs at higher In mole fraction. The decrease in the V_{oc} for the devices with InAs quantum dots is due to decrease in the band gap of the solar cell as the In mole fraction is increased. Other possibilities for the decrease are charge trapping and recombination in the quantum dots. The defects formed during the growth of self-assembled InAs quantum dots can act as centers of Auger recombination that are detrimental to the performance of the solar cell. Similar decrease in V_{oc} in InAs quantum dot solar cells was reported by Hubbard *et al* [19]. The power conversion efficiency of the quantum dot/quantum well solar cells is found to be in the range of 5 % - 8 %, which is smaller than that of the reference GaAs pn junction solar cell.

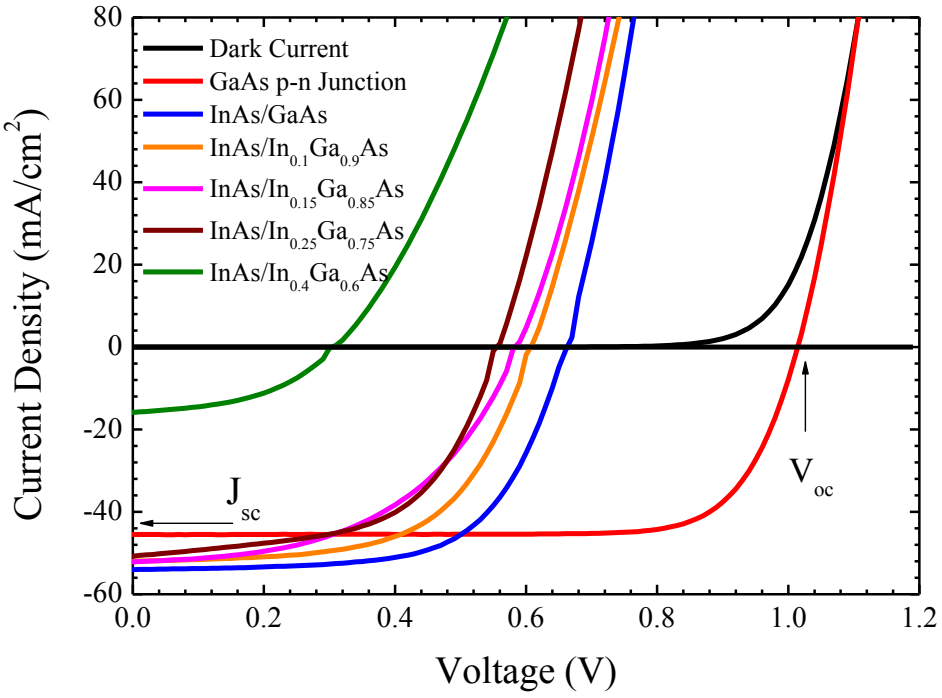

Figure 4.5 IV characteristics of InAs/InGaAs devices are plotted along with the reference GaAs pn junction solar cell.

In mole fraction (x)	J_{sc} (mA/cm^2)	V_{oc} (V)	η (%)	FF
0	50.5	0.66	7.6	0.64
10	52.5	0.60	6.3	0.60
15	52.6	0.58	5.1	0.50
25	52.0	0.55	5.4	0.57
40	15.9	0.31	0.75	0.45

Table 4.1 Power conversion efficiency, short circuit current density, open circuit voltage, and fill factor of InAs/ $In_xGa_{1-x}As$ solar cells are tabulated as a function of x.

4.2 Anti-reflection coating for GaAs solar cells

4.2.1 Introduction

As discussed earlier an ideal antireflection coating for a GaAs solar cell should have a refractive index equal to:

$$n_{ARC} = \sqrt{n_{air} n_{GaAs}} \tag{4.2}$$

where, n_{ARC} is the refractive index of antireflection coating, n_{air} is the refractive index of air and n_{GaAs} is the refractive index of GaAs. Zinc Oxide (ZnO) is a semiconductor, which has a refractive index of 1.6 to 1.8 in the wavelength range of 400 nm to 800 nm. The band gap of ZnO is ~ 3.4 eV. Hence, it is transparent to most of the wavelengths above 380 nm. These parameters make ZnO a perfect ARC for GaAs solar cells.

4.2.2 Deposition and Characterization of film

In this project, ZnO synthesized by sol gel technique was deposited on the GaAs solar cells as an ARC. The ZnO sol gel was spin coated using Brewer Science 200K spin coating system. The deposited films were annealed in a vacuum furnace to remove all the organic compounds from the sol gel leaving behind a thin film of ZnO.

The refractive index of GaAs, ZnO film measured using spectroscopic ellipsometry is shown in the figure 4.6. Also, the refractive index for an ideal ARC calculated from equation 4.2 is plotted. It is evident from the plot that the refractive index of ZnO film is close to the ideal ARC for GaAs substrates. The extinction coefficient of ZnO ARC and GaAs substrates, plotted as a function of wavelength, is shown in figure 4.7. The extinction coefficient or the imaginary part of refractive index indicates the amount of absorption through the material as the light

passes through it. It can be seen that the extinction coefficient of ZnO film is almost zero in the visible region. These optical parameters and thickness of the ZnO ARC film were measured using spectroscopic ellipsometry. A GaAs substrate with 2.23 nm of oxide layer was used as the model to fit the Ψ and Δ values measured from the ellipsometer. The optical constants and oxide layer thickness was fit to the model with a mean squared error (MSE) of 3.22. A Cauchy model was used to fit the optical constants and thickness of the ZnO ARC layer. The Ψ and Δ values in this case was fit with a MSE of 26.56.

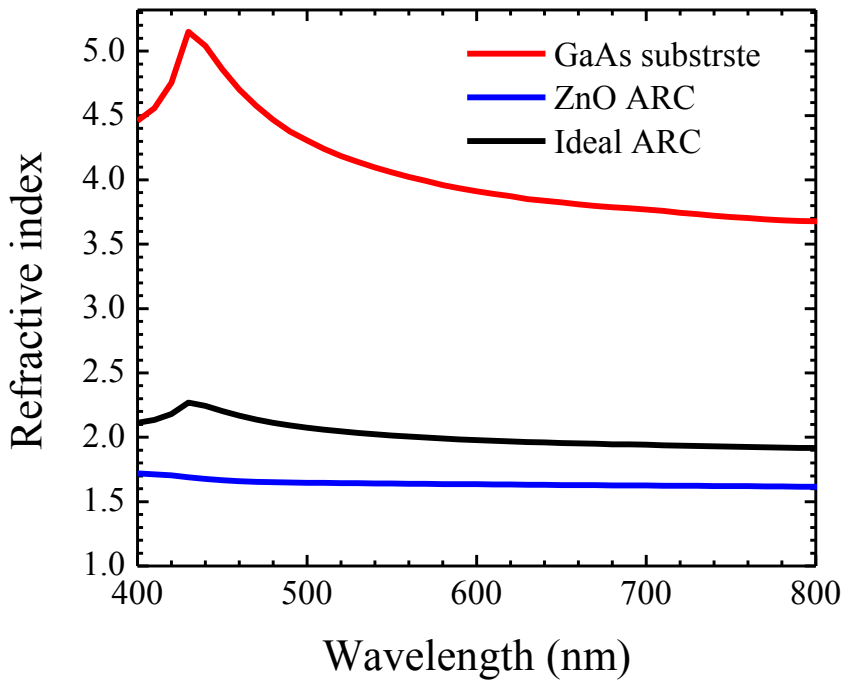

Figure 4.6 Refractive index of ZnO film is compared with the calculated refractive index of an ideal ARC for GaAs substrates.

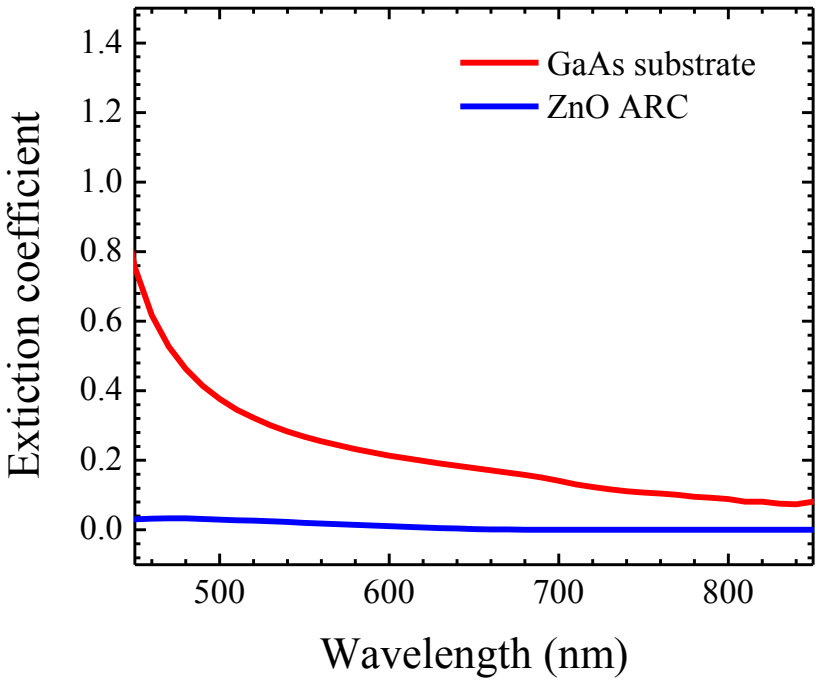

Figure 4.7 Extinction coefficients of GaAs and ZnO film are plotted as a function of wavelength of incident light.

The deposited film was first characterized by using X-ray diffraction (XRD) system to confirm the presence of ZnO. The results of XRD of ZnO film spin coated on GaAs substrate is shown in figure 4.8. The results obtained were compared to a materials library to identify the peaks seen in the XRD graph. The peaks at 37.4^{o} and 43.7^{o} indicated by arrows in the graph correspond to ZnO. The broader peak at 65.8^{o} corresponds to GaAs crystal, which is the substrate. As seen from the figure the GaAs peak is suppressed when compared to the ZnO. This is possible by performing an offset scan instead of a normal scan in the XRD. By performing a scan at an offset angle of about ~ 3^{o}, the peak from the substrate can be avoided. In this case the substrate is a single crystal GaAs and the lattice points are avoided by doing the offset scan.

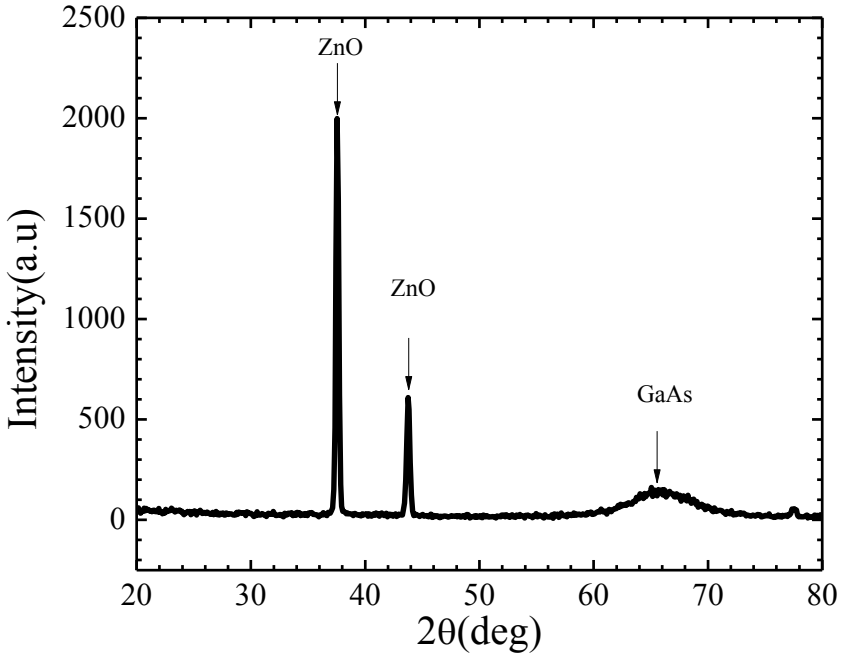

Figure 4.8 XRD peaks showing the presence of ZnO in the ARC film on GaAs substrate.

In order to verify the anti-reflective property, the ZnO sol gel was coated on undoped GaAs and the transmission was measured using a UV-Vis spectrophotometer. The ZnO sol gel was spin coated at different speeds and annealed. The transmission of pristine undoped GaAs and the GaAs with ZnO coating plotted as a function of wavelength of incident light is shown in figure 4.9. As seen from the figure the transmission of light through GaAs has been substantially increased after the application of ZnO film. The transmission of pristine GaAs is around ~53 % in the wavelength range of 1800 nm and 2800 nm. In the same wavelength range the transmission of GaAs with ZnO film is around ~61%. This serves as an indication that ZnO film acts as an ARC on GaAs substrates. The sharp decline in transmission seen in the curves is due to the absorption by the GaAs substrate above its band gap. Moreover, the transmission is higher and more uniform for films spin coated at 8000 rpm and 10000 rpm. The thickness of the film deposited is ~111 nm at 8000 rpm and ~100 nm at 10000 rpm.

The transmission results give only an indication that the ZnO film is working as an ARC. To confirm the anti-reflective property of ZnO, reflectance was measured using spectroscopic ellipsometer. The reflectance measurement was made at an incident angle of 15^{o}. The reflectance of pristine GaAs and GaAs samples coated with ZnO at 8000 rpm and 10000 rpm is shown in figure 4.10. The reflectance was considerably reduced after ZnO deposition. It decreased from 35 % to 3 % at 600 nm. The average decrease in the 400 nm to 800 nm wavelength range is ~ 30 %. Also the film spin coated at 10000 rpm showed better anti-reflective property than the film coated at 8000 rpm. This is due to the lesser thickness of the film deposited at 10000 rpm.

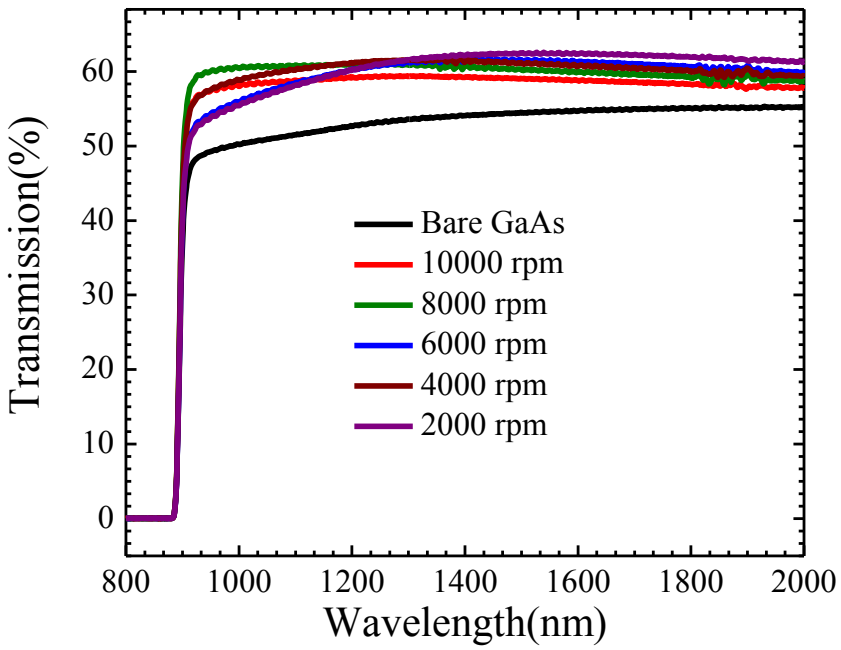

Figure 4.9 Transmission spectra of undoped GaAs samples with ZnO ARC spin coated at different speeds.

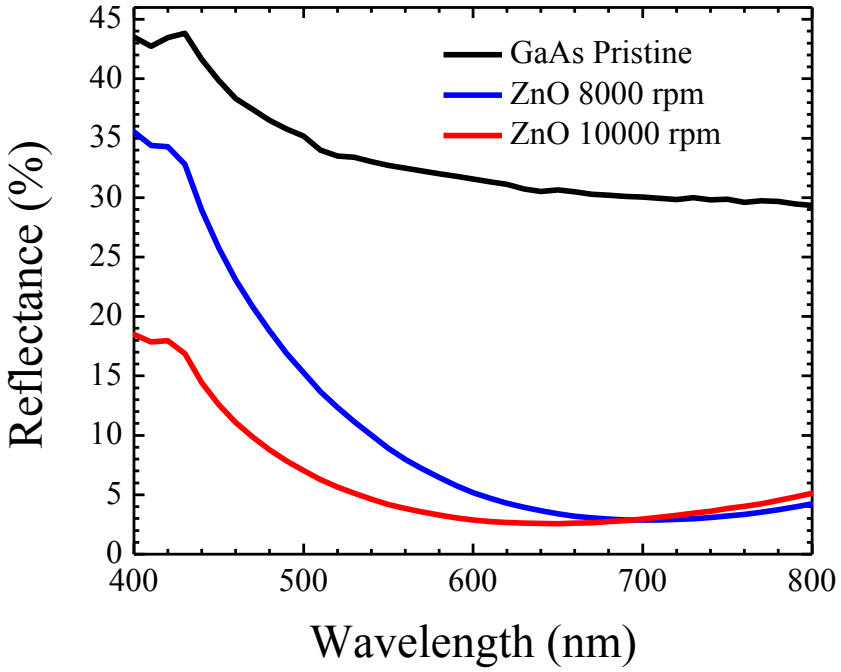

Figure 4.10 Reflectance of light from pristine GaAs and GaAs coated with ZnO ARC measured at an angle of incidence of 15^{o}.

4.2.3 Optimization of ARC films

The coating speed was optimized by depositing the ZnO films on GaAs pn junction solar cells and measuring the IV characteristics. These solar cells were fabricated from the same wafer and were processed together under same conditions. The relative increase in efficiency and increase in J_{sc} after deposition of ARC plotted as a function of coating speed are shown in figure 4.11. It can be noted that the solar cell coated at 10000 rpm performed the best. The relative efficiency increase was about 31 % and the increase in J_{sc} was 17.0 mA/cm^2. The annealing temperature was chosen as 150 ^{o}C. At this temperature most of the organic materials in the sol – gel evaporate leaving ZnO. Moreover, annealing at high temperature for a prolonged period damages the solar cell and thus degrading the performance.

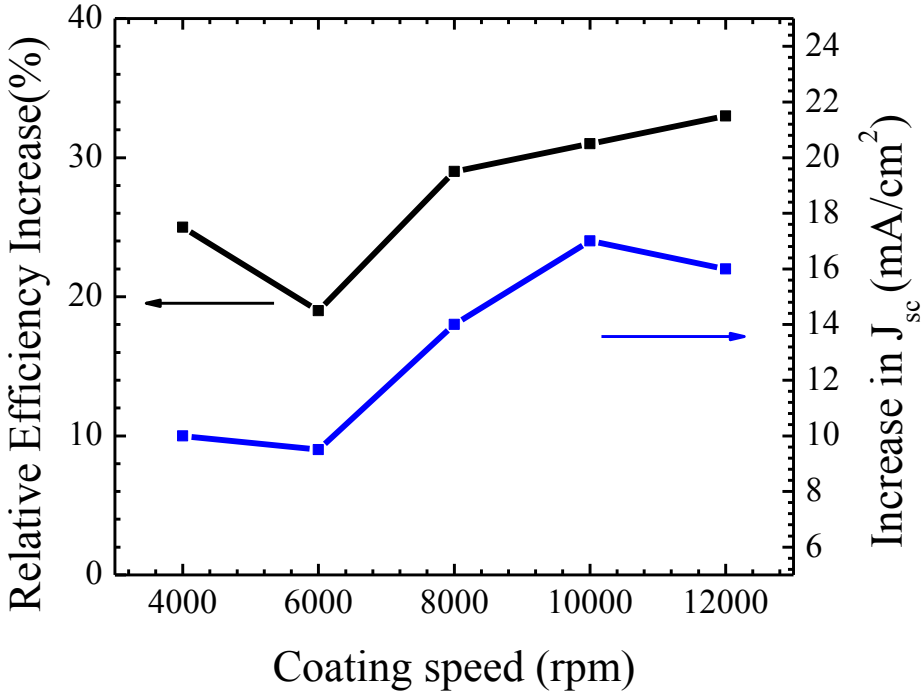

Figure 4.11 Performance of GaAs pn junction devices are plotted as a function of ARC film coating speed.

4.2.4 InAs/GaAs solar cells with ZnO ARC

The ZnO synthesized using sol-gel method was spin coated on InAs quantum dot solar cells and the performance was evaluated before and after deposition. The InAs quantum dots were grown by MBE using Stranski-Krastanov growth mode. Ten periods of 2ML InAs quantum dots in a GaAs barrier was grown on an n-type GaAs substrate. The InAs quantum dots were doped with [Si] = $2x10^{17}$ cm^{-3}. An n-type GaAs buffer layer was grown on top of the substrate, which was doped with [Si] = $5x10^{18}$ cm^{-3}. The InAs/GaAs structure was capped with a p-type GaAs cap layer doped with [Be] = $1x10^{18}$ cm^{-3}. An n-type $Al_{0.2}Ga_{0.8}As$ doped with [Si] = $1x10^{18}$ cm^{-3} was inserted in the buffer layer. A 40 nm p-type $Al_{0.85}Ga_{0.15}As$ doped with

[Be] = $1x10^{18}$ cm^{-3} was inserted in the cap layer which acts as the window layer. The solar cells were fabricated in a class 100 clean room using the procedure discussed in previous chapters. The n-type contact was made of AuGe/Ni/Au with a thickness of 75 nm/20 nm/100 nm. The p-type contact was made of Au/Zn/Au with a thickness of 100 nm/20 nm/100 nm.

The solar cells fabricated were first cleaned with 6 % HCl to remove the gallium oxide and arsenous oxide formed on the surface. Then the devices were again rinsed with a stream of acetone and methanol to remove any organic impurities form the surface. The cleaned solar cells were coated with ZnO at 10000 rpm for 30 sec. The IV characteristics of the solar cell measured using AM1.5G, 3 sun solar simulator is shown in the figure 4.12. The relative increase in power conversion efficiency after ARC deposition is around ~29 %. The J_{sc} increased from 50 mA/cm^2 to 69 mA/cm^2 and the V_{oc} remained the same. It can be noted that the fill factor decreased from 0.60 to 0.57, which is due increased leakage current. This shows that the increase in efficiency is mainly due to increase in J_{sc}. This shows that the enhancement in performance is due to ARC because an ideal ARC increases the J_{sc} without affecting the V_{oc}.

The EQE of the InAs quantum dot solar cell was measured between 400 nm and 1000 nm and is plotted in figure 4.13 (a). The average increase in EQE after ARC deposition in the wavelength range of 500 nm to 850 nm was found to be 31 %. The maximum increase of about 43 % was seen at a wavelength of 700 nm after ARC deposition. It can also be noted that presence of ZnO ARC has enhanced the peak at 920 nm. This extended response is due to interband transition within the InAs quantum dots. Similar kind of enhancement was also seen in the spectral response of the solar cell. The spectral response of the device between 400 nm and 1200 nm, measured using a FTIR spectrometer, is shown in figure 4.13 (b). The peak at 867 nm is due to the interband transition in the GaAs. The smaller peak at 920 nm is due to the interband

transition within the InAs quantum dot, as these peaks are not present in the GaAs pn junction solar cell. The spectral response exhibits an enhancement over the entire wavelength range after ARC deposition. The maximum relative enhancement is around 43 % at 867 nm

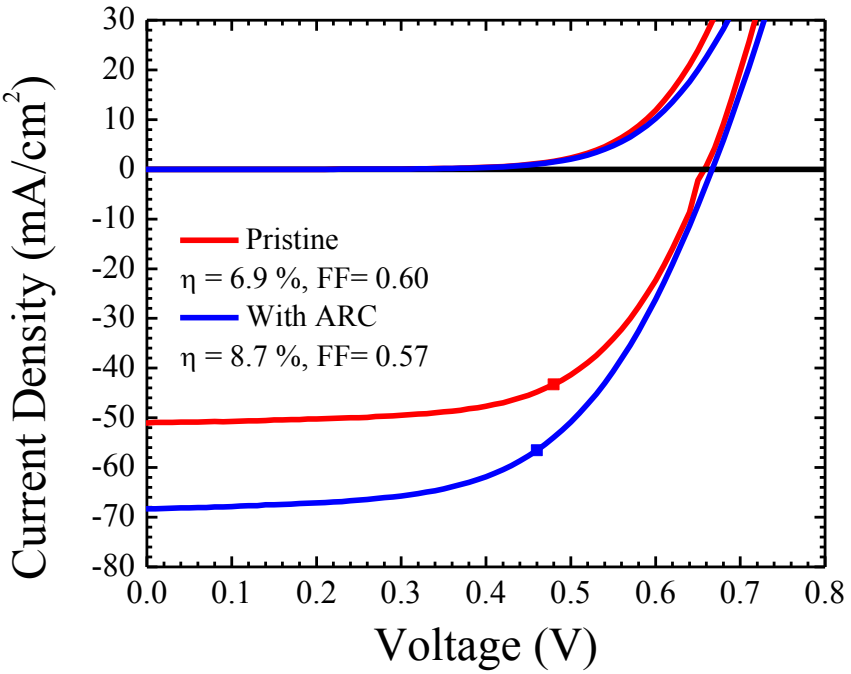

Figure 4.12 Current-Voltage characteristics of InAs/GaAs solar cell showing the enhancement after ZnO ARC deposition.

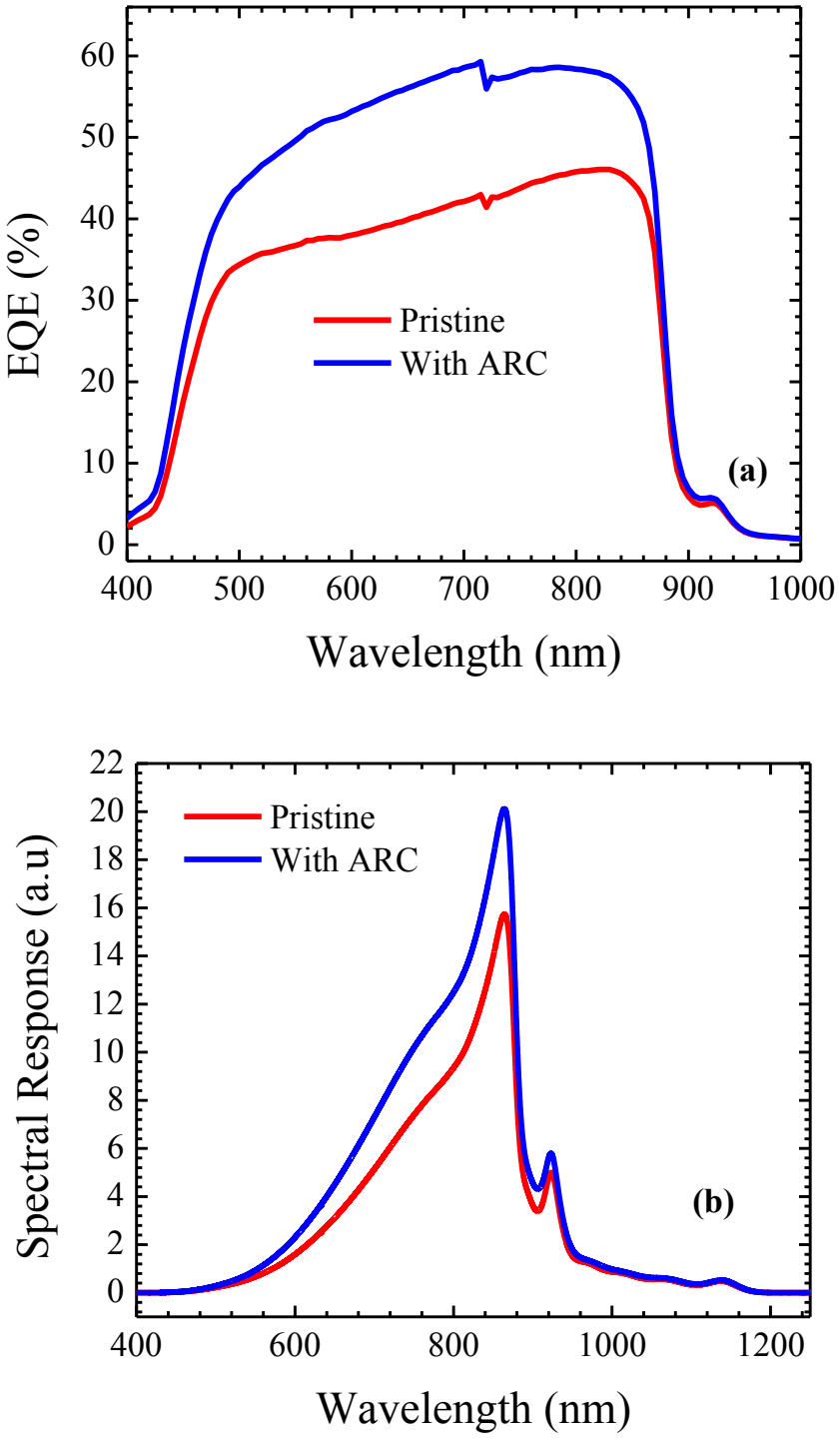

Figure 4.13 (a) Enhancement in EQE and (b) enhancement in spectral response of InAs/GaAs solar cell after ZnO ARC deposition.

4.2.5 InAs/$In_{0.15}Ga_{0.85}As$/GaAs solar cells with ZnO ARC

The ZnO ARC was also deposited on InAs/$In_{0.15}Ga_{0.85}As$/GaAs solar cell to investigate the performance. Ten periods of 2ML InAs quantum dots/5nm of $In_{0.15}Ga_{0.85}As$ quantum well/35nm GaAs barrier structure was grown on an n-type GaAs substrate. The InAs quantum dots were doped with [Si] = $2x10^{17}$ cm^{-3}. An n-type GaAs buffer layer was grown on top of the substrate, which was doped with [Si] = $5x10^{18}$ cm^{-3}. The InAs/$In_{0.15}Ga_{0.85}As$/GaAs structure was capped with a p-type GaAs cap layer doped with [Be] = $1x10^{18}$ cm^{-3}. An n-type $Al_{0.2}Ga_{0.8}As$ doped with [Si] = $1x10^{18}$ cm^{-3} was inserted in the buffer layer. A 40 nm p-type $Al_{0.85}Ga_{0.15}As$ doped with [Be] = $1x10^{18}$ cm^{-3} was inserted in the cap layer which acts as the window layer. The solar cells were fabricated in a class 100 clean room using the procedure discussed in previous chapters. The n-type contact was made of AuGe/Ni/Au with a thickness of 75 nm/20 nm/100 nm. The p-type contact was made of Au/Zn/Au with a thickness of 100 nm/20 nm/100 nm.

The solar cells fabricated were first cleaned with 6 % HCl and dried using nitrogen. Then the devices were again rinsed with a stream of acetone and methanol to remove any organic impurities form the surface. The cleaned solar cells were coated with ZnO at 10000 rpm for 30 sec. The IV characteristic of the solar cell before and after ARC deposition is shown in figure 4.14. The power conversion efficiency exhibited a relative increase of 42 % after the ARC deposition. The enhancement is mainly due to increase in J_{sc}, which increased from 47 mA/cm^2 to 69 mA/cm^2. The EQE measured between 400 nm to 1100 nm wavelength range is shown in figure 4.15 (a). The average relative enhancement in the 500 nm to 850 nm range is ~ 43 %. Similar enhancement is also seen in the spectral response measurement shown in figure 4.15 (b). The peak at 920 nm seen in both EQE and spectral response is due to the InAs quantum dot. The peak at 965 nm due to the interband transition within the $In_{0.15}Ga_{0.85}As$ quantum well. Both

these peaks exhibit significant enhancement after ARC deposition. The enhancement at these higher wavelength shows that the ARC is active over a wide wavelength range.

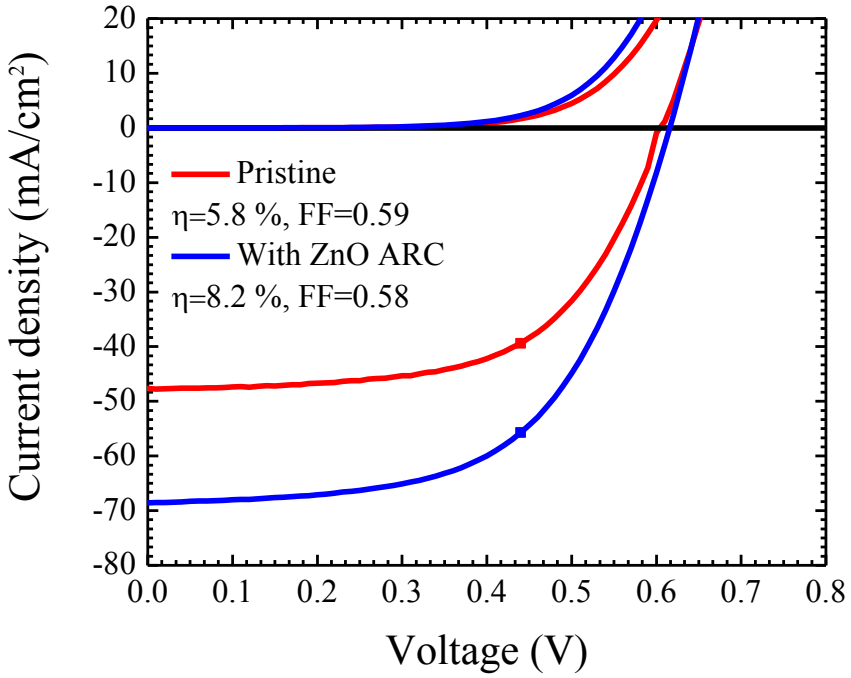

Figure 4.14 Enhancement in the IV characteristics of InAs/ $In_{0.15}Ga_{0.85}As$ quantum dots in well solar cell with ZnO ARC.

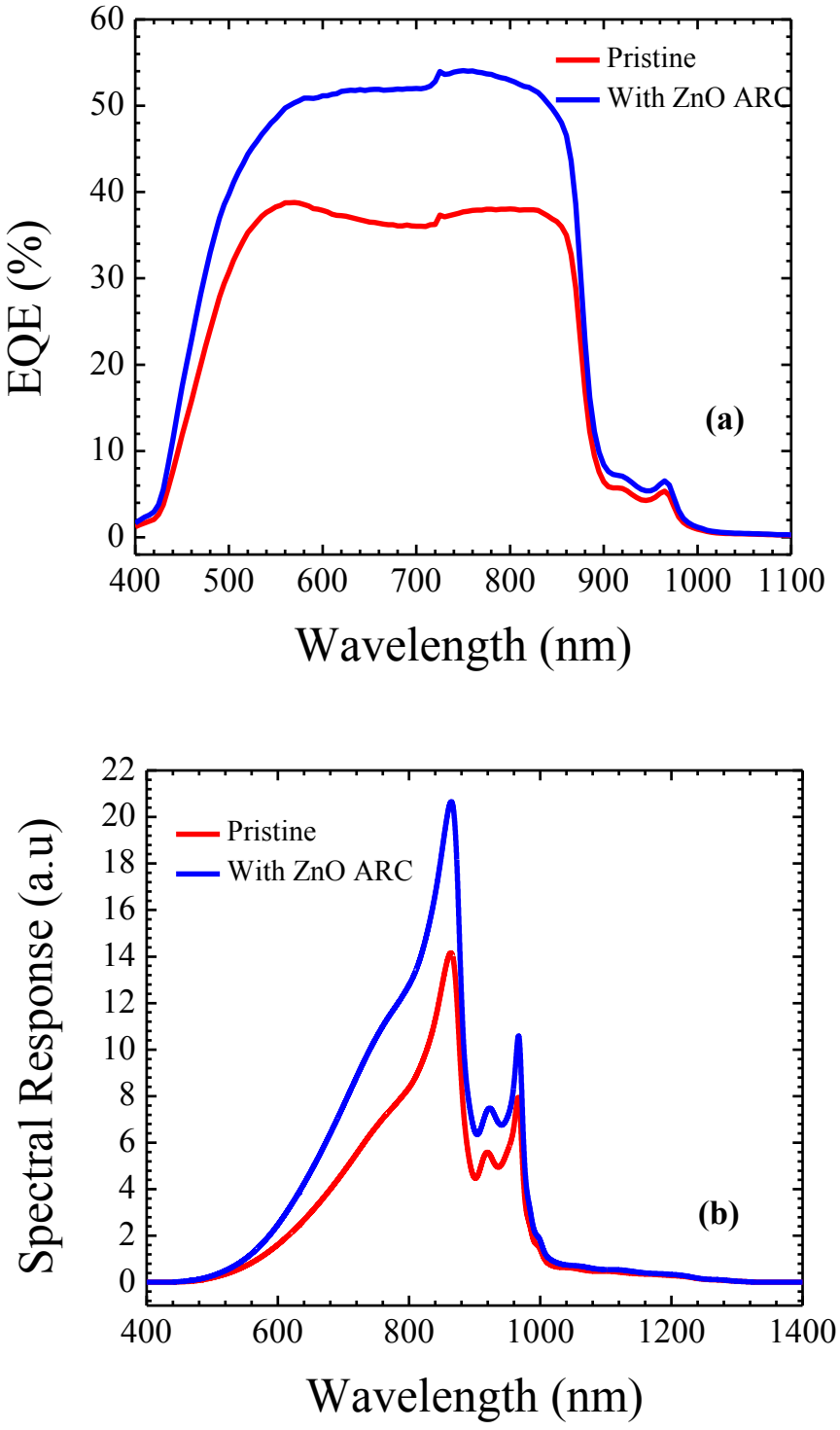

Figure 4.15 (a) Quantum efficiency and (b) spectral response enhancement in InAs/$In_{0.15}Ga_{0.85}As$ quantum dots in well solar cell with ZnO ARC.

5. CONCLUSION AND FUTURE WORK

5.1 Conclusion

In conclusion, the performance of InAs/$In_xGA_{1-x}As$/GaAs solar cells as a function of x has been evaluated. The solar cells were fabricated using chemical wet etching process in aclean room. The performance was evaluated by using the IV characteristics, external quantum efficiency and spectral response measurements. The results exhibit extended response in the near infrared region of the spectrum as x is increased. There is some enhancement in the J_{sc} due to interband transitions associated with quantum dots and quantum wells. But the overall power conversion efficiency of these devices is less when compared to GaAs pn junction devices. The decrease in efficiency is attributed to the strain induced dislocation caused by the lattice mismatch between InAs and GaAs.

In order to increase the efficiency of these solar cells, ZnO ARC films were deposited on the surface. The ZnO was prepared by sol-gel method and spin coated on the solar cells. The ZnO ARC films on GaAs substrates were characterized extensively using XRD, ellipsometry, transmission and reflectance measurements. The performance of the solar cells enhanced significantly after ARC deposition. The power conversion efficiency and quantum efficiency measurements exhibited an enhancement of 42 % and 43 % respectively.

5.2 Future Work

The extended infra-red response seen in the InAs quantum dots embedded in InGaAs quantum wells solar cell indicate that there is potential to obtain high efficiency. The increase in short circuit current density is encouraging, but the efficiency obtained so far is less. This is due to the reduced open circuit voltage caused by defects in the structures. These defects are the

result of strain induced between InGaAs and GaAs. One way to reduce the strain is by engineering the device structure effectively by introducing strain reducing layers. The use of ZnO/MgF_2 bilayer anti-reflection coating, multilayer anti-reflection coating with graded refractive indices can increase the light trapping ability of solar cell and enhance the efficiency further.

REFERENCES

1. M. Green, *Solar Cells: Operating Principles, Technology, and System Applications*. Englewood Cliffs, NJ: Prentice Hall, 1982.

2. A. Luque and S. Hegedus, *Handbook of Photovoltaic Science and Engineering*. Chichester, West Sussex, UK: John Wiley & Sons Ltd., 2011.

3. R.W. Miles, K.M. Hynes, and I. Forbes, "Photovoltaic solar cells: An overview of state-of-the-art cell development and environmental issues", *Prog. in Cryst. Grow. and Charact. of Mat.*, vol. 51, pp. 1-42, 2005.

4. J.J. Loferski, "Theoretical Considerations Governing the Choice of the Optimum Semiconductor for Photovoltaic Solar Energy Conversion," *J. of Appl. Phys.*, vol. 27, pp. 777-784, 1956.

5. L.M. Fraas and L.D. Partain, *Solar Cells and Their Applications*. Hoboken, NJ: John Wiley & Sons, Inc., 1995.

6. R.H. Bube, *Photovoltaic Materials.* London, UK: Imperial College Press, 1998.

7. A.R. Gobat, M.F. Lamorte, and G.W. McIver, "Characteristics of High-Conversion-Efficiency Gallium-Arsenide Solar Cells,"*IRE Trans. on Milit. Electron.,* vol. 6, pp. 20-27,1962.

8. D. A. Jenny, J. J. Loferski, and P. Rappaport, "Photovoltaic effect in GaAs p-n junctions and solar energy conversion," *Phys. Rev.*, vol. 101, pp. 1208-1209, 1956.

9. J.J. Loferski, "Tandem Photovoltaic Solar Cells and Increased Solar Energy Conversion Efficiency," *Proceedings of the 12th IEEE Photovoltaics Specialists Conference*, Baton Rouge, LA, 1976, pp. 957-960.

10. N.A. Gokcen, J.J. Loferski, "Efficiency of tandem solar cell systems as a function of temperature and solar energy concentration ratio," *Sol. Energy Mat.,* vol. 1, pp. 271-286, 1979.

11. W. Shockley, H. J. Queisser, "Detailed Balance Limit of Efficiency of pn Junction Solar Cells," *J. Appl. Phys.*, vol. 32, 510-519, 1961.

12. G. L. Araujo, and A. Marti, "Absolute Limiting efficiencies for photovoltaic energy conversion," *Sol. Eng. Mat. Sol. Cells*, vol. 33, pp. 213-240, 1994.

13. A. Luque, and A. Marti, "Increasing the Efficiency of Ideal Solar Cells by Photon Induced Transitions at Intermediate Levels," *Phys. Rev. Lett.*, vol. 78, pp. 5014-5017, 1997.

14. A. Luque, and A. Marti, "The Intermediate Band Solar Cell: Progress Toward the Realization of an Attractive Concept," *Adv. Mat.*, vol. 22, pp. 160-174, 2010.

15. L. Cuadra, A. Marti, and A. Luque, "Influence of the Overlap Between the Absorption Coefficients on the Efficiency of the Intermediate Band Solar Cell," *IEEE Trans. Electron Dev.*, vol. 51, pp. 1002 - 1007, 2004.

16. A. Luque, A. Martí, C. Stanley, N. López, L. Cuadra, D. Zhou, and A. Mc-Kee, "General equivalent circuit for intermediate band devices: Potentials, currents and electroluminescence," *J. Appl. Phys.*, vol. 96, pp. 903-909, 2004.

17. S. A. Blokhin, A. V. Sakharov, A. M. Nadtochy, A. S. Pauysov, M. V. Maximov, N. N. Ledentsov, A. R. Kovsh, S. S. Mikhrin, V. M. Lantratov, and S. A. Mintairov, "AlGaAs/GaAs Photovoltaic Cells with an Array of InGaAs QDs," *Semiconductors*, vol. 43, pp. 514-518, 2008.

18. J. Wu, Y. F. M. Makableh, R. Vasan, M. O. Manasreh, and B. Liang, "Strong interband transitions in InAs quantum dots solar cell," *Appl. Phys. Lett.*, vol. 100, pp. 1907-1910, 2012.

19. S. M. Hubbard, C. D. Cress, C. G. Bailey, R. P. Raffaelle, S. G. Bailey, and D. M. Wilt, "Effect of strain compensation on quantum dot enhanced GaAs solar cells," *Appl. Phys. Lett.*, vol. 92, pp. 3512-3514, 2008.

20. C. G. Bailey, D. V. Forbes, R. P. Raffaelle, and S. M. Hubbard, "Near 1 V open circuit voltage InAs/GaAs quantum dot solar cells," *Appl. Phys. Lett.*, vol. 98, pp. 3105-3107, 2011.

21. A. Hospodkova, E. Hulicius, J. Oswald, J. Pangrac, T. Mates, K. Kuldova, K. Melichar, and T. Simecek, "Properties of MOVPE InAs/GaAs quantum dots overgrown by InGaAs," *J. Cryst. Growth*, vol. 298, pp. 582-585, 2007.

22. D. Zhou, G. Sharma, S. F. Thomassen, T. W. Reenaas, and B. O. Fimland, "Optimization towards high density quantum dots for intermediate band solar cells grown by molecular beam epitaxy," *Appl. Phys. Lett.*, vol. 96, pp. 1913-1915, 2010.

23. K. Laouthaiwattana, O. Tangmattajittakul, S. Suraprapapich, S. Thainoi, P. Changmuang, S. Kanjanachuchai, S. Ratanathamaphan, and S. Panyakeow, "Optimization of stacking high-density quantum dot molecules for photovoltaic effect," *Sol. Eng. Mat. Sol Cells*, vol. 93, pp. 746-749, 2009.

24. G. Wei and S. R. Forrest, "Intermediate-Band Solar Cells Employing Quantum Dots Embedded in an Energy Fence Barrier," *Nano Lett.*, vol. 7, pp. 218-222, 2006.

25. D. Hu, C. McPheeters, E. T. Yu, and D. M. Schaadt, "Improvement of performance of InAs quantum dot solar cell by inserting thin AlAs layers," *Nanoscale Res. Lett.*, vol. 6, pp. 83-87, 2011.

26. Y. C. Lee, C. C. Chang, and Y. Y. Chou, "Experimental and simulation studies of anti-reflection sub-micron conical structures on a GaAs substrate," *Opt. Exp.*, vol. 21, pp. A36-A41, 2013

27. Z. I. Alexieva, Z. S. Nenova, V.S. Bakardjieva, M. M. Milanova, H. M. Dikov, "Antireflection coatings for GaAs solar cell applications," *J. of Phys.: Conf. Ser.*, vol. 223, pp. 2045-2048, 2010

28. P. Yu, C. H. Chang, C.H. Chiu, C.S. Yang, J.C. Yu, H. C. Kuo, S. H. Hsu, and Y. C. Chang, "Efficiency enhancement of GaAs photovoltaics employing antireflective indium tin oxide nanocolumns," *Adv. Mat.,* vol. 21, pp. 1618-1621, 2009

29. M. O. Manasreh, *Semiconductor heterojunctions and nanostructures*. New York, NY: McGraw Hill, 2005.

30. I. Kamiyaa, I. Tanakab, O. Ohtsukic, H. Sakakib, "Density and size control of self-assembled InAs quantum dots: preparation of very low-density dots by post-annealing," *Phys. E*, vol. 13, pp. 1172-1175, 2002.

31. M.N. Kamalasanan, S. Chandra, "Sol-gel synthesis of ZnO thin films," *Thin Sol. Films*, vol. 288, pp. 112-115, 1996.

32. R. C. Perez, O. J. Sandoval, S. J. Sandoval, J. M. Marin, A. M. Galvan, G. T. Delgado, and A. M. Alvarez, " Influence of annealing temperature on the formation and characteristics of sol-gel prepared ZnO films," *J. Vac. Sci. Technol. A*, vol. 17, pp. 1811-1816, 1999.

33. M. F. Malek, M. H. Mamat, M. Z. Sahdan, M. M. Zahidi, Z. Khusaimi, M. R. Mahmood," Influence of various sol concentrations on stress/strain and properties of ZnO thin films synthesised by sol–gel technique" *Thin Sol. Films*, vol. 527, pp. 102–109, 2013.

34. J. H. Lee, K. H. Ko, B. O. Park," Electrical and optical properties of ZnO transparent conducting films by the sol–gel method, " *J. of Cry. Gro.*, vol. 247, pp. 119–125, 2003.

35. C. Y. Huang, C. Y. Cheng, C. Y. Huang, Y. K. Su, and C. L. Fang, "Efficiency Improvements of GaAs-based Solar Cells by Hydrothermally-deposited ZnO Nanostructure Array," *World Acad. of Sci., Eng. & Tech.*, vol. 79, pp. 1009-1013, 2011.

36. A. G. Bacaa, F. Renb, J. C. Zolpera, R. D. Briggsa, and S. J. Peartonc, " A survey of ohmic contacts to III-V compound semiconductors," *Thin Sol. Films*, vol. 308-309, pp. 599-606, 1997.

37. A. Lopez, A. Marti, A. Luque, C. Stanley, C. Farmer, and P. Diaz, "Experimental analysis of the operation of quantum dot intermediate band solar cells," *J. of Sol. Energy Eng.,* vol. 129, pp. 319-322, 2007.

38. R. E. Nahory, M. A. Pollack, W. D. Johnston, and R. L. Barns, "Band gap versus composition and demonstration of Vegard's law for $In_{1-x}Ga_xAs_yP_{1-y}$ lattice matched to InP " *Appl. Phys. Lett.*, vol. 33, pp. 659-661, 1978.

39. X. J. Shang, J. F. He, H. L. Wang, M. F. Li, Y. Zhu, Z. C. Niu, Y. Fu, "Effect of built-in electric field in photovoltaic InAs quantum dot embedded GaAs solar cell " *Appl. Phys. A.* vol. 103, pp. 335-337, 2011.